Strongly nonlinear multi-degree of freedom systems
Experimental analysis and model identification

Martinelli, Cristiano; Coraddu, Andrea; Cammarano, Andrea

Important note
To cite this publication, please use the final published version (if applicable).
Please check the document version above.

Strongly nonlinear multi-degree of freedom systems: Experimental analysis and model identification

Cristiano Martinelli [a,c,*], Andrea Coraddu [b], Andrea Cammarano [c]

[a] *University of Strathclyde, Department of Naval Architecture, Ocean and Marine Engineering, 100 Montrose Street, Glasgow, G4 0LZ, Scotland, United Kingdom*
[b] *TU Delft, Department of Maritime and Transport Technology, Mekelweg 2, CD Delft, 2628, The Netherlands*
[c] *University of Glasgow, James Watt School of Engineering, James Watt South Building, Glasgow, G12 8QQ, Scotland, United Kingdom*

ARTICLE INFO

ABSTRACT

Lightweight structures, once ubiquitous in specific sectors such as aeronautics and space sectors, in recent years, have increasingly attracted the attention of industries that, historically, have not been particularly concerned with structural weight. Ample examples are provided by the civil and automotive industry, in which the paradigm shift towards lower carbon footprint and sustainability prompted new trends characterised by mass reduction, the use of novel materials, and the accounting for large deformations. However, accurately modelling the dynamic behaviour of such structures requires nonlinear mathematical models, which are not widely used in common industrial practices. Reduced-Order Models (ROMs) have emerged as a popular alternative to computationally expensive Finite Element (FE) models, nonetheless, there is still a need to evaluate their effectiveness in accurately modelling strongly nonlinear behaviours.

This study investigates the capacity of multiple-degree-of-freedom (MDOF) ROMs to capture and predict the nonlinear behaviour of lightweight structures subjected to large deformations. A novel identification procedure, built on existing linear and nonlinear identification methods, is used to identify an ROM from numerical and experimental data. Being based on the separation of the linear and nonlinear restoring force contributions, the proposed method can be easily embedded in the current industrial practices for the identification of mechanical systems, paving the way to an integrated usage of linear and nonlinear dynamic models. To validate the identified MDOF-ROM, a lightweight structure composed of lumped masses and nonlinear elastic connections is experimentally studied and the numerical and experimental results are compared at different excitation conditions. We demonstrated that the existence of the Nonlinear Restoring Force (NLRF) surface in a reduced subspace corresponds to the presence of local active nonlinearities in the experimental model. This information permits simplifying the nonlinear restoring force function of the ROM, improving the overall identification process. Finally, we showed that the identified ROM accurately represents the nonlinear dynamic behaviour of the experimental test rig and correctly predicts the passage from high-amplitude response to low-amplitude response (jumps) when different levels of excitation are applied to the system, demonstrating the effectiveness of the proposed procedure.

1. Introduction

Lightweight structures have been largely adopted in the aerospace industry for the design and manufacturing of spacecraft and satellites. This choice is driven by the necessity to reduce the weight, a good cost predictor [1], to satisfy the limited mass and volume budgets allocated to space missions [2]. In recent years, however, industrial sectors that have historically privileged strength in favour of weight, like the automotive, power, civil, and transport industries have shown increasing interest in the adoption of lightweight structures and systems, as testified by the increasing usage of composite material in the automotive sector [3]. This natural trend towards lighter structures is driven by the need to face technological problems that emerged with the strict CO2 policies [4,5], nowadays implemented by many countries, which aim to reduce emissions. For example, in the civil sector, the usage of lightweight high-performance systems would reduce material utilisation and would lower the CO2 emissions associated with the production and transportation of raw materials. Likewise, in the transport industry, the utilisation of lighter vehicles would reduce fuel consumption and emissions [6]. On the contrary, in the energy sector, lighter structures would help to solve technological problems, allowing further increases in the maximum dimension of wind turbines [7]. In this case, lightweight structures and materials may allow facing the presence of increasing inertia and gravity loads in large wind turbine blades, reducing their overall weight and boosting wind turbine energy production. Nonetheless, high-performance lightweight structures may show nonlinear behaviours in the operational range; typical examples come from the aerospace industry where nonlinear structural dynamic behaviours have been observed for a long time. For instance, Cassini spacecraft [8] and Airbus A400M aircraft [9] showed typical nonlinear behaviours during classical experimental ground vibration tests. In addition, many numerical studies have demonstrated the possibility of triggering geometric nonlinearities in lightweight systems and structures at relatively low forcing levels [10–14]. This undermines the classical linear assumption adopted in the majority of the industrial practices for modelling the dynamic behaviour of mechanical systems and makes it more difficult to perform dynamic simulations. Despite the existence of numerical techniques, e.g., nonlinear Finite Element Analysis (FEA), modelling complex systems results in a computational burden that increases exponentially with the number of Degrees of Freedom (DOFs), which makes unpractical the investigation of the full dynamics of a nonlinear structure. This represents a major issue for industries that must perform multiple simulations and investigate the system dynamics in diverse scenarios, like in the certification phase of new aerospace solutions.

Reduced-order modelling represents a promising methodology for reducing the computational cost of dynamic nonlinear analyses: this procedure tries to reduce the active DOFs of a nonlinear model by imposing, identifying, or selecting a certain number of master DOFs, thus reducing the complexity of the system and improving the computational burden of simulations [12,15–17]. Such methods are particularly suitable for lightweight flexible structures which show geometric nonlinear behaviour when subjected to large deformation [12]. Touzé et al. [17] recently reviewed the various methodologies for reducing the order of nonlinear systems based on the invariant manifold theory. The theory was originally applied to vibratory systems by Shaw and Pierre [18–20] and it is based on the Centre Manifold Theorem and the Lyapunov Subcentral Manifold Theorem [21,22] which guarantee the existence and the uniqueness of a centre manifold. Nonetheless, the theory and associated theorems hold only for undamped unforced systems (conservative systems). Recent developments of Haller et al. [23] have extended this concept to non-conservative systems, i.e., systems with damping and forcing terms, introducing the notion of Spectral Sub-manifold (SSMs). As shown by Touzé et al. [17], reduced order models can be obtained from either Partial Differential Equations (PDEs), e.g. with the Graph or Normal Form Styles [18–20,24–26], or from FE models, e.g. with the Implicit Condensation and Expansion (ICE) [16,27], Stiffness Evaluation Procedure (STEP) [28,29] and Direct Normal Form (DNF) method [15]. Therefore, ROMs represent a possible way to reduce the computational burden of nonlinear dynamic simulations, easing the usage of numerical continuation and integration schemes; nevertheless, most of the reduced models have been studied, compared, and verified only in numerical studies. The scientific literature features a few examples of using ROMs for the identification of experimental nonlinear systems [30–32]. Noël et al. [30] proposed a procedure based on the Frequency-domain Nonlinear Subspace Identification (FNSI) method [33] for identifying the Nonlinear Normal Modes (NNMs) of mechanical structures. In [30], the authors adopted a FE model to prove the capabilities of the proposed procedure; after having identified a state-space reduced model, they showed that the NNMs, as frequency-amplitude plots, can be correctly retrieved from experimental data, which were generated from a numerical model. Denis et al. [31] adopted a reduced model based on the normal form of the equation of motions. The resulting ROM was used to identify the parameters of different nonlinear systems from experimental backbone curves. Jossic et al. [32] performed the identification of the conservative parameters of a Chinese gong featuring pitch glide and softening stiffness behaviour. They adopted the same procedure proposed in [31] to identify a ROM and they compared the experimental backbone curves obtained by exciting one NNM or multiple NNMs, capturing with their ROM the pitch glide which is mainly due to the nonlinear behaviour of the system. Czaplewski et al. [34] experimentally analysed a MEMS resonator featuring a 1:3 internal resonance. The authors demonstrated that a simple Duffing oscillator coupled with a linear oscillator can correctly describe the bifurcation diagram of the MEMS under investigation. Other works that adopt reduced models for identifying/visualising the response of the system can be found in [35–37]. In most of the aforementioned works, ROMs are utilised to identify the system parameters from experimental measurements. The method can be only applied to conservative systems [21,22] or systems where the damping contribution is negligible, and thus, direct identification of the damping parameters cannot be achieved. This prevents us from verifying the ROM capacities to predict jumps and changes of stability, i.e., to check all the phenomena typically connected to damping. Therefore, it is not possible to assess to what extent the identified model is representative of the system dynamics. Finally, the identification of MDOF ROMs is generally avoided because, as demonstrated in many numerical examples [38,39], the behaviour of these systems may be extremely complicated even with few degrees of freedom. This is further complicated by the presence of internal resonances [40,10] and energy exchanges between

Table 1

Longitudinal distance between the components of the experimental model. The directions are expressed considering the triad shown in Fig. 1.

Component	S_1–M_1	M_1–M_2	M_2–S_2
Longitudinal distance (X)	85.0 mm	165.0 mm	85.0 mm.

non-resonant modes with unlocked phase [41] when certain forcing conditions are applied to the system. In these cases, using ROMs with few DOFs may not capture the system dynamics, being unable to model internal resonances and bifurcation scenarios correctly.

In the literature, many other identification methods for nonlinear systems have been proposed since the 60s; Kerschen, Noël and collaborators [40,42] reviewed different methods, providing guidelines for their usage. Between them, the Restoring Force Surface (RFS) method has been identified as one of the most effective methods since its presentation by Masri and Caughey [43]. Authors have also proposed different versions of the RFS method and applied it in many examples, which spaces from energy harvesters to real satellites. Bonisoli and Vigliani [44] adopted the RFS method to identify experimentally the nonlinear parameters of a passive magneto-elastic suspension. Cammarano et al. [45] successfully applied the RFS method to extract the nonlinear properties of a bistable vibration energy harvester, while Rizos et al. [46] applied the method to leaf-spring-based tuned mass damper. In a more complex real-life scenario, Noël et al. [47] utilised the RFS method for the identification of trilinear characteristics associated with a Wheel Elastomer Mounting System (WEMS) of a small real satellite. The authors demonstrated that the identified system is able to correctly reproduce the nonlinear behaviour of the WEMS with good accuracy, even in such a complex structure. In another real case scenario, Kerschen et al. [10] applied the RFS method to identify the nonlinear characteristics between the aircraft wings and fuel tanks. The author successfully identified the nonlinear properties and adopted them to perform a numerical analysis of the NNMs associated with a ROM. Recently, Anastasio et al. [48] utilised the RFS method to identify the nonlinear stiffness properties of a Duffing-like negative stiffness oscillator. All these examples demonstrate the good capabilities of the method and its reliability in the identification of nonlinear properties.

This paper proposes a novel identification procedure for MDOF ROMs representing nonlinear systems. The procedure, named the Nonlinear Restoring Force (NLRF) method, represents a modified version of the RFS method [49,50] and it is based on the assumption that the restoring force is composed of linear and nonlinear components. This concept is certainly not new to the scientific literature [51–53], nonetheless, unlike other methods, the proposed methodology allows obtaining a graphical representation of the nonlinear restoring force, even in the case of MDOF systems. This has the intrinsic advantage of showing the minimal dimensional space that fully describes the nonlinear behaviour of the system, i.e., it shows if the nonlinear restoring force depends on the coordinates of one or more DOFs. In the case of localised nonlinearities, this allows for simplifying the definition of the unknown nonlinear function, reducing its complexity. In addition, thanks to the separation of linear and nonlinear restoring forces, the proposed method can be interfaced with well-established identification methods for linear systems, paving the way to a more integrated use of nonlinear identification methods in industrial practices. A lightweight structure consisting of lumped masses and flexible connectors is experimentally investigated and then used to prove the capabilities of the proposed approach and the associated ROM. To this end, the identified MDOF-ROM is assessed in terms of the capacity to capture and predict the nonlinear dynamic behaviour of the experimental test rig. Thanks to the graphical nature of the proposed method, the restoring force of localised active nonlinearities is shown to exist in a reduced subspace, providing additional insight into the dynamics of the system. This information is then used to model the nonlinear contributions of the system and identify the nonlinear dynamic behaviour of the experimental test rig. The identified ROM is validated against different sets of experimental data, demonstrating that it is capable of capturing the dynamics of the experimental system in the investigated amplitude–frequency ranges.

2. Experimental analysis of the nonlinear multi-degree of freedom system

This section introduces the results of the experimental analysis: firstly, the experimental set-up and the model are described in detail, and then the results of the experimental campaign are shown and commented. The presented experimental data are available for download from the following repository [54].

2.1. Experimental set-up and test-rig

The experimental test-rig wants to represent a lightweight structure with multiple DOFs subjected to large deformations. It is constituted of two parallel slender beams (section 20 mm × 0.5 mm) with a scale that indicates their length, two rigid supports, and two main masses. The supports and the masses are made in Poly-Active Lacyd (PLA), a common material adopted for 3D printing, while the beams are in stainless steel. The parallel configuration of the beams provides a hardening nonlinear characteristic to the experimental system: when the mass is displaced from its resting position, the beams experience both bending and axial deformation. The latter produces axial stress, which has the effect of increasing the bending stiffness of the beams, providing the nonlinear restoring force. As shown in Fig. 1, the masses and the beams are kept in the desired position thanks to the force exercised by the external transparent closure parts in polymethyl methacrylate. These transparent parts allow setting the position of the mass precisely, exploiting the scale marked on the beams. The longitudinal distances between the masses and the supports adopted in this study are reported in Table 1. Table 2, instead, reports the dimensions of the main components constituting the experimental model in the X, Y, and Z directions as reported in Fig. 1. The experimental model is mounted on a vibrating table, which is excited
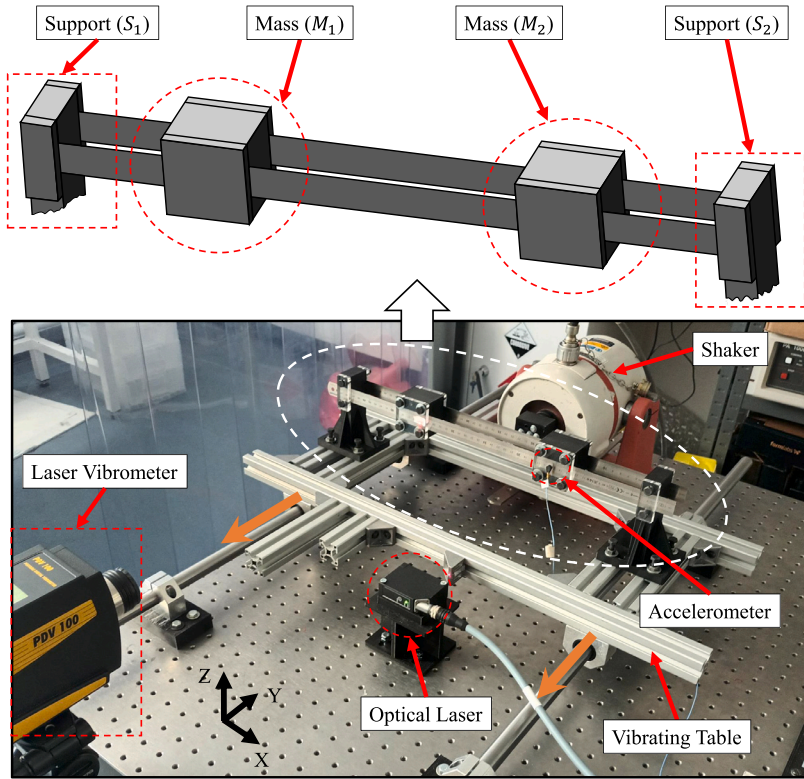
Fig. 1. Experimental test rig representing a lightweight nonlinear structure featuring large deformations. The orange arrows represent the direction of excitation of the vibrating table. A schematic drawing of the considered system is reported in the upper part of the figure.

Table 2
Dimension of the experimental system components. The directions are expressed considering the triad shown in Fig. 1.

Component	Length (x-direction)	Width (y-direction)	Height (z-direction)
Beam	500 mm	0.5 mm	20 mm.
Mass	50 mm	47.5 mm	50 mm

by a shaker (LDS-V403). The table permits the motion of the system only in the direction transversal to the longitudinal axis of the model (Y direction according to the reference system reported in Fig. 1). During the measurement campaign, two lasers and an accelerometer were used to measure the displacement, velocity, and acceleration of different points of the test rig: a single-point laser vibrometer (Polytec PVD 100) is used to record the velocity of the first mass (M_1), while an accelerometer (PCB Piezotronics Model: 352C22) is adopted to measure the acceleration of the second mass (M_2). The motion of the vibrating table, instead, is measured with a single-point optical laser (Micro-Epsilon optoNCDT 1402), which works as a feedback sensor for controlling the amplitude of displacement of the base. To this end, a feedback control loop is implemented in the test rig by using the control unit dSPACE (CP1104). The idea is to exploit the control system to remove the dynamics of the shaker from the signal, thus avoiding interferences that may modify the dynamics of the system [55,56]. A schematic representation of the control architecture is reported in Fig. 2: the control unit measures the displacement of the vibrating table (d_{base}), the velocity of the first mass (v_{M_1}), and the acceleration of the second mass (a_{M_2}) which are then displayed as output variables for inspection. The displacement signal is filtered, and a Root Mean Square (RMS) online function is adopted to control its amplitude: this function provides an estimation of the amplitude of the fundamental harmonic of sinusoidal-like signals, as the one produced by the vibrating table. By controlling the RMS of the signal, the control effort is drastically reduced and the comparison with numerical results obtained from perfect sinusoidal excitation is possible, as demonstrated by previous studies [57,45]. A proportional–integral–derivative controller (PID) controller is then used to modulate the amplitude signal that will be passed to the shaker and a saturation function defines a limit threshold for the amplitude. Finally, the signal generator produces a sinusoidal voltage signal at the desired frequency ($\bar{d}_{frq}$) which is passed to the shaker.

2.2. Experimental data acquisition

The experimental setup described in Section 2.1 is now used to measure the dynamic response of the system. Firstly, the underlying linear behaviour of the system is measured by using a signal analyser (Data Physics - Abacus 901). The signal analyser
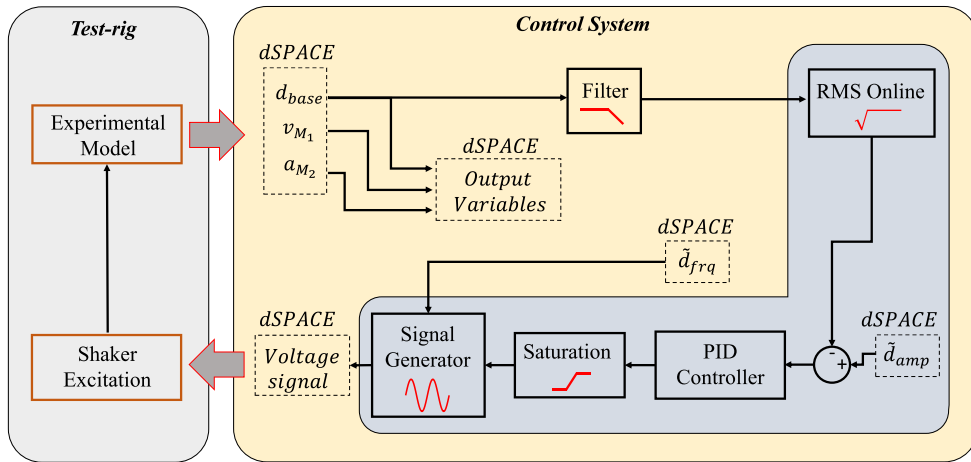
Fig. 2. Schematic representation of the control architecture adopted in the experimental set-up. Dashed boxes denote the input/output signals of the dSPACE. Quantities $\tilde{d}_{frq}$ and $\tilde{d}_{amp}$ denote, respectively, the imposed frequency and amplitude.
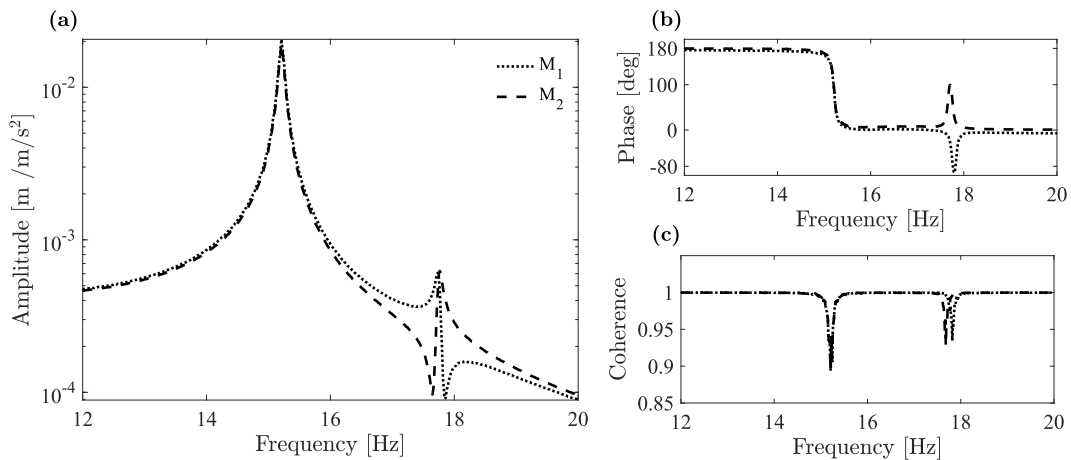

Fig. 3. Averaged experimental FRF, representing the underlying linear system. The transfer function is obtained with the random low-amplitude input signal and it is described in terms of amplitude (a) and phase (b). The coherence of the measured signal (c) is also reported for completeness.

adopts a commercial code (SignalCalc 900 Series) and, by converting the data from time to frequency domain, provides an averaged Frequency Response Function (FRF). In order to identify the underlying linear behaviour, the system is excited with low amplitude random excitation [58,59], limiting the effect of smooth nonlinearities. At low levels of amplitude, it is not expected to experience any mode bifurcation [40], therefore the identification of an underlying linear system can be considered to be achievable. Fig. 3(a–b) shows the underlying linear FRF, expressed as amplitude and phase of the receptance between the motion of the base and the displacement of the masses. The transfer function shows the presence of the first two modes of the system in the range between 12-20 Hz with the first mode showing the largest amplitude of response: this dynamic response is due to the type of excitation that mainly excites the first mode. Fig. 3(c), instead, shows the coherence of the measured FRF; high levels of coherence are recorded for the considered spectrum of excitation, with the minimum values equal to 0.89, for the first mode, and 0.92, for the second mode. The high coherence in the signals is an indication of the statistical robustness and the repeatability of measurement, demonstrating that the measured FRF, at this level of excitation, presents very limited nonlinear behaviours only near the resonance peaks.

To trigger the nonlinear behaviour, large amplitude frequency sweeps are applied to the experimental test rig. The response of the system is measured in the time domain and subsequently post-processed to obtain the Frequency Response Curve (FRC), i.e., the nonlinear response of the system in the frequency domain. The analysis is performed by controlling the amplitude of the displacement of the vibrating table and it is repeated for three different excitation levels, namely, 0.03 mm, 0.04 mm, and 0.05 mm. The frequency range investigated varies from 14.5 Hz to 19.5 Hz. The FRC is measured with a discrete variation of excitation frequency of 0.1 Hz: for each frequency, the excitation signal is maintained for 45 seconds to let the transient response die. The time signal is then filtered with a high pass filter (2 Hz) and a low pass filter (150 Hz) and divided into chunks of 45 seconds where the excitation has a well-defined constant frequency. Then, the transient response is removed, and the steady-state signal is used to
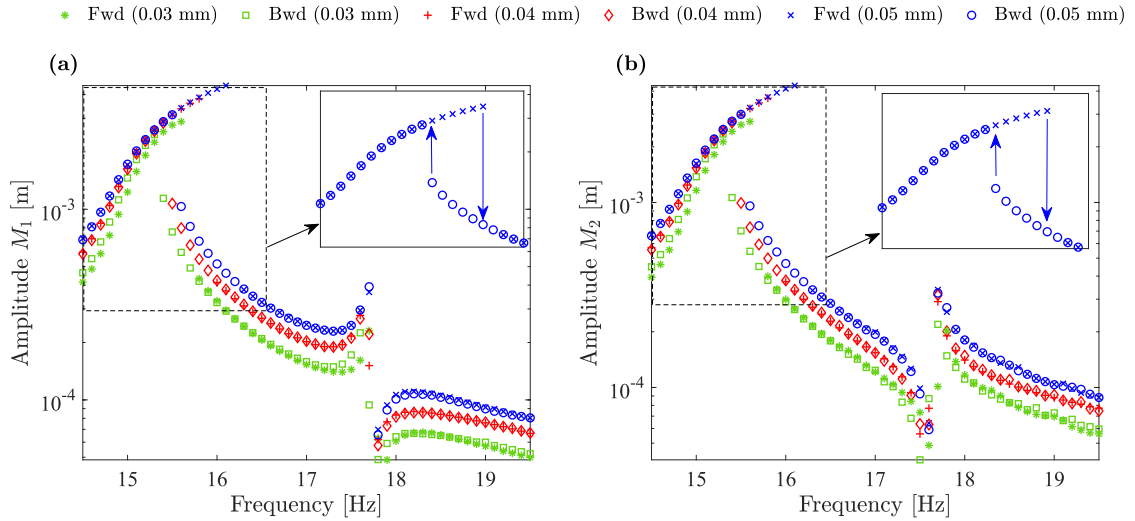
Fig. 4. Experimental frequency response curve of the system in the nonlinear regime. The FRCs are obtained with forward (Fwd) and backward (Bwd) discrete frequency sweeps and they are described in terms of displacement of the first (a) and the second mass (b). Different colours indicate different levels of base excitation amplitude, i.e. 0.03 mm (green), 0.04 mm (red), and 0.05 mm (blue).

compute the amplitude of the response at each frequency. To ensure robustness, the response amplitude is obtained by averaging the amplitudes associated with each period of the steady-state signal. Fig. 4 shows the FRC of the nonlinear system for the three investigated excitation conditions. The PID controller ensures a smooth and gradual change in the excitation frequency, allowing the system to be maintained within specific conditions until the jumps between high- and low-amplitude of response occurs. This results in the typical hysteresis loop of a nonlinear system that is reported in the details of Figs. 4(a) and 4(b). As expected, the nonlinear behaviour of the system is of the hardening type; this is confirmed by the resonance peaks of the frequency response, shown to be bent towards higher frequencies. It is worth noting that there is good agreement between the forward and backward amplitudes of response away from the hysteresis loop, demonstrating the robustness of the experimental analysis.[1]

Table 3 provides an overview of the accuracy of the controller and reports the mean and the standard deviation of the measured vibrating table amplitude for each experimental measurement. The mean and standard deviation are obtained from a vector of amplitudes which can be computed at each excitation frequency with the following expression:

$$A_{vt}(\Omega) = \sqrt{2}\sqrt{\frac{1}{n}\sum_{i=1}^{P} x_{vt}(t_i)^2},$$ (1)

where $A_{vt}(\Omega)$ is the amplitude of the vibrating table at a certain frequency, $x_{vt}(t_i)$ represents the ith component of the associated time history (displacement), and P is the number of elements of the considered time history. In particular, Eq. (1) represents the amplitude computed as the RMS of a perfect sinusoid which is here utilised to estimate the amplitude of the vibrating table at a specific frequency of excitation. The computed amplitudes, along the entire sweep, are then utilised to obtain the mean and standard deviations for each measurement. The results of Table 3 demonstrate that the measured input amplitudes are very close to the imposed ones (reported in brackets) in all the experiments, confirming the accuracy of the controller. In addition, the standard deviation is very low, showing that there are small variations of the input amplitude along the different frequency sweeps. It is worth noting that the forward frequency sweep experiments have a slightly higher standard deviation than the backward ones. This phenomenon is due to the presence of large amplitudes of response, especially near the jumps, which demand high control effort.

3. Parameters identification via nonlinear restoring force method

This section introduces and applies the proposed identification process to the experimental system. The procedure tries to create a bridge between the well-established linear identification methods, which already find applications in industrial practices, and nonlinear methods. A schematic flowchart of the proposed procedure is reported in Fig. 5. In the first phase, the underlying linear behaviour of the system is experimentally analysed and utilised to select a proper ROM. Then, by utilising well-established linear identification methods, the linear parameters of the selected system are estimated and optimised. The second phase of the process aims to identify the nonlinear behaviour of the system; to this end, the NLRF method is introduced and utilised to identify a

---

[1] The computation of confidence bands at 99% of confidence highlighted that the standard deviation is at least 5 orders of magnitude smaller than the mean of the measurements. Given such a high confidence level, the confidence bands are not reported in Fig. 4.

Table 3

Experimental displacement amplitudes of the vibrating table. The displacement amplitude of the signal is computed with Eq. (1) and it is reported in terms of mean and standard deviation considering the entire frequency sweep.

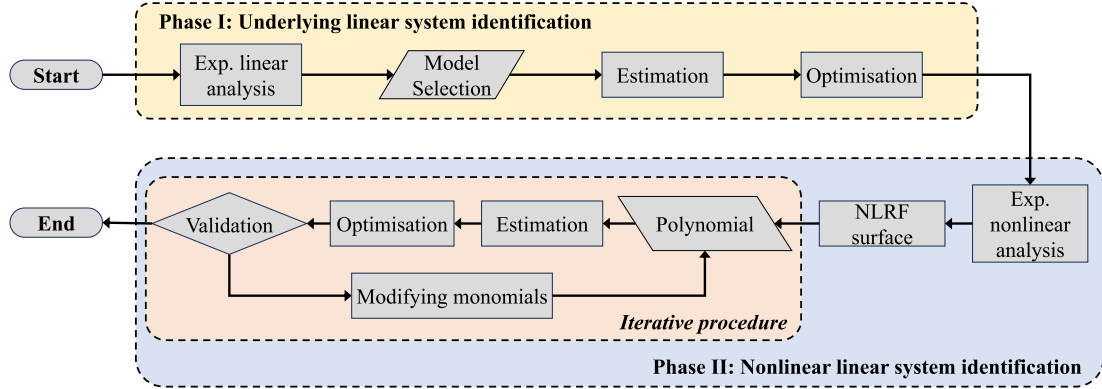| Measurement	Mean	Standard deviation
Forward sweep (0.03 mm)	3.02×10^{-5} m	1.47×10^{-6} m
Backward sweep (0.03 mm)	3.01×10^{-5} m	2.48×10^{-8} m
Forward sweep (0.04 mm)	4.00×10^{-5} m	1.03×10^{-6} m
Backward sweep (0.04 mm)	4.02×10^{-5} m	3.11×10^{-8} m
Forward sweep (0.05 mm)	5.01×10^{-5} m	6.41×10^{-7} m
Backward sweep (0.05 mm)	5.02×10^{-5} m	3.81×10^{-8} m

Fig. 5. Flowchart of the proposed identification procedure. The two main phases (linear and nonlinear identification) are denoted by different blocks.

polynomial function representing the nonlinear contribution of the system. There, a systematic iterative procedure is followed to identify the nonlinear restoring force function. The section concludes with a numerical example and the model validation against different sets of experimental data.

3.1. Identification of the underlying linear system

The identification of a ROM representing the underlying linear behaviour of the system is performed with well-established identification techniques, which are typically used for the identification of linear systems (e.g., 3 dB method, circle fit method [58]): the advantage of these methods consists in the fact that they are simple, reliable, commonly available and accessible, and very well-known in industrial procedures. Often, similar methods are already implemented in commercial software for signal processing and, thus, they are easily applicable to both simple and complex structures. The selection of an appropriate ROM is a critical choice in every system identification procedure, even when the nonlinear behaviour of the investigated mechanical structure can be neglected [58]. In experimental modal analysis, stabilisation diagrams may help to identify a suitable ROM for the measured FRFs, distinguishing between physical and fictitious modes. Nonetheless, the final choice of the ROM is ultimately delegated to the practitioner. In this study, we utilise a straightforward practical approach: the experimental analysis, described in Section 2 has shown the presence of two modes in the frequency range 0–40 Hz, hence, a two-DOFs system is selected as a ROM for the identification procedure. This is motivated by the fact that the linear identification will provide two natural frequencies and two damping ratios. The model is schematically represented in Fig. 6 where m represent the mass, k_1, k_2, k_3 are the linear stiffness coefficients, c_1, c_2, c_3 denote the linear damping coefficients, while μ_1, μ_2, μ_3 and δ_1, δ_2, δ_3 are the nonlinear stiffness and damping coefficients. This system wants to be as general as possible, and it can be mathematically represented by the following set of ODEs:

$$m\ddot{z}_1 + c_1\dot{z}_1 + c_2(\dot{z}_1 - \dot{z}_2) + k_1 z_1 + k_2(z_1 - z_2) + N_{RF,1}(z_1, z_2, \dot{z}_1, \dot{z}_2) = -m\ddot{y} \tag{2a}$$

$$m\ddot{z}_2 + c_3\dot{z}_2 - c_2(\dot{z}_1 - \dot{z}_2) + k_3 z_2 - k_2(z_1 - z_2) + N_{RF,2}(z_1, z_2, \dot{z}_1, \dot{z}_2) = -m\ddot{y} \tag{2b}$$

where y represents the base displacement, $z = x - y$ indicates the relative displacement between the base and the masses, and $N_{RF,1}$ and $N_{RF,2}$, instead, define the nonlinear restoring terms associated with the first and second DOF. The identification of the linear coefficients of Eq. (2) is performed by exploiting the experimental linear transfer functions represented in Fig. 3; the natural frequencies ω_n, modal damping ratios ζ, and the modal matrix Ψ of MDOF mechanical systems are extracted with the previously cited methods [58]. The obtained modal properties can be then organised in a matrix form as follows:

$$\mathbf{D} = \begin{bmatrix} 2\zeta_1\omega_{n,1} & 0 \\ 0 & 2\zeta_2\omega_{n,2} \end{bmatrix} \tag{3a}$$
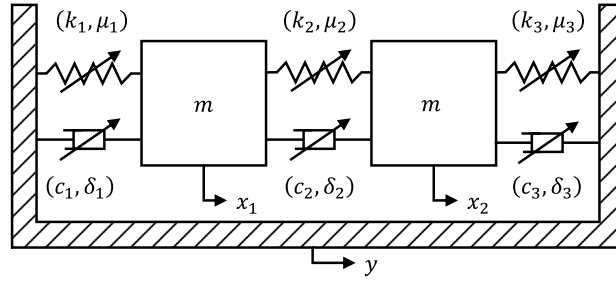
Fig. 6. Reduced order model with two degrees of freedom representing the experimental model of Fig. 1. The arrows indicate the presence of nonlinear behaviour in the connecting element.

Table 4
Linear coefficients identified from the experimental linear transfer function. The first line denotes the linear coefficients obtained from Eq. (4) (established identification methods) while the second line represents the linear coefficients obtained after the optimisation procedure.

Coefficients	c_1 [Ns/m]	c_2 [Ns/m]	c_3 [Ns/m]	k_1 [N/m]	k_2 [N/m]	k_3 [N/m]
Estimated	0.0727	0.0256	0.0750	1235.8	225.3	1256.3
Optimised	0.0582	0.0205	0.0600	1232.9	225.1	1261.9

$$\mathbf{W}_n = \begin{bmatrix} \omega_{n,1}^2 & 0 \\ 0 & \omega_{n,2}^2 \end{bmatrix} \tag{3b}$$

where $\mathbf{D}$ and $\mathbf{W}_n$ are the matrices of the damping ratios and natural frequencies. The modal matrices are then converted into physical matrices by using the procedure outlined in previous works [55] and here reported for completeness. The mass matrix $\mathbf{M}$ can be represented with a diagonal matrix composed of the masses of M_1 and M_2 which have been experimentally measured equal to 0.1365 kg. Then, the damping $\mathbf{C}$, and stiffness $\mathbf{K}$ matrices can be obtained with following mathematical expressions:

$$\mathbf{C} = \begin{bmatrix} c_1 + c_2 & -c_2 \\ -c_2 & c_2 + c_3 \end{bmatrix} = (\boldsymbol{\Psi}^T)^{-1}(\boldsymbol{\Psi}^T \mathbf{M} \boldsymbol{\Psi} \mathbf{D})(\boldsymbol{\Psi})^{-1} \tag{4a}$$

$$\mathbf{K} = \begin{bmatrix} k_1 + k_2 & -k_2 \\ -k_2 & k_2 + k_3 \end{bmatrix} = (\boldsymbol{\Psi}^T)^{-1}(\boldsymbol{\Psi}^T \mathbf{M} \boldsymbol{\Psi} \mathbf{W}_n)(\boldsymbol{\Psi})^{-1} \tag{4b}$$

Eq. (4) allows obtaining an estimation of the coefficients representing the underlying linear system, as illustrated in phase I of Fig. 5. Nonetheless, such an estimation requires improvement. For this reason, an iterative optimisation procedure is adopted, and the estimated linear coefficients are used as an initial guess. An optimisation algorithm aims at minimising the difference between the experimental and the analytical transfer functions in terms of amplitude and phase. This helps to mitigate the errors that the identification of the modal matrix of the underlying linear system may introduce. The outlined identification process adopts the MATLAB minimisation function named: *lsqnonlin*, this function implements the classical Levenberg–Marquardt algorithm which is suitable for similar minimisation problems. In this work, the receptance is adopted as a reference transfer function for the minimisation procedure, and its analytical representation can be expressed as follows:

$$H_1 = \frac{X_1}{\ddot{Y}} = \frac{X_2 k_2 - \frac{\ddot{Y} k_1}{\Omega^2} + \Omega X_2 c_2 i - \frac{\ddot{Y} c_1 i}{\Omega}}{\ddot{Y}\left(k_1 + k_2 - \Omega^2 m + \Omega\left(c_1 + c_2\right) i\right)} \tag{5a}$$

$$H_2 = \frac{X_2}{\ddot{Y}} = \frac{X_1 k_2 - \frac{\ddot{Y} k_3}{\Omega^2} + \Omega X_1 c_2 i - \frac{\ddot{Y} c_3 i}{\Omega}}{\ddot{Y}\left(k_2 + k_3 - \Omega^2 m + \Omega\left(c_2 + c_3\right) i\right)} \tag{5b}$$

where, X_1 and X_2 are the complex amplitudes of the absolute displacements of M_1 and M_2, $\ddot{Y}$ represents the complex amplitude of the acceleration input, and Ω denotes the forcing frequency of the excitation. The results of the optimisation procedure are reported in Table 4: the first line describes the linear coefficients obtained with the circle fit and half power methods while the second line reports the optimised coefficients. The optimisation process led to the refinement of coefficients, resulting in a more precise representation of the measured dynamic behaviour. Although these coefficients differ slightly from the original ones, the similarity demonstrates the ability of classical methods to provide a good estimate of such parameters. Fig. 7 compares the experimental and analytically optimised transfer functions. The response of the first DOF is reported in the left panels, while the right panels describe the behaviour of the second DOF. The upper panels describe the amplitude response along the investigated frequency range, instead, the lower panels illustrate the phase associated with the considered degree of freedom. The analytical results show a good fitting with the experimental data, demonstrating that the optimised coefficients and the selected ROM capture the dynamic behaviour of the experimental system in the linear regime.

The simple design used in the test rig allows for the direct measurement of the masses. When this is not possible, an alternative approach consists in evaluating the system mass by assessing the changes in the natural frequencies caused by adding known mass
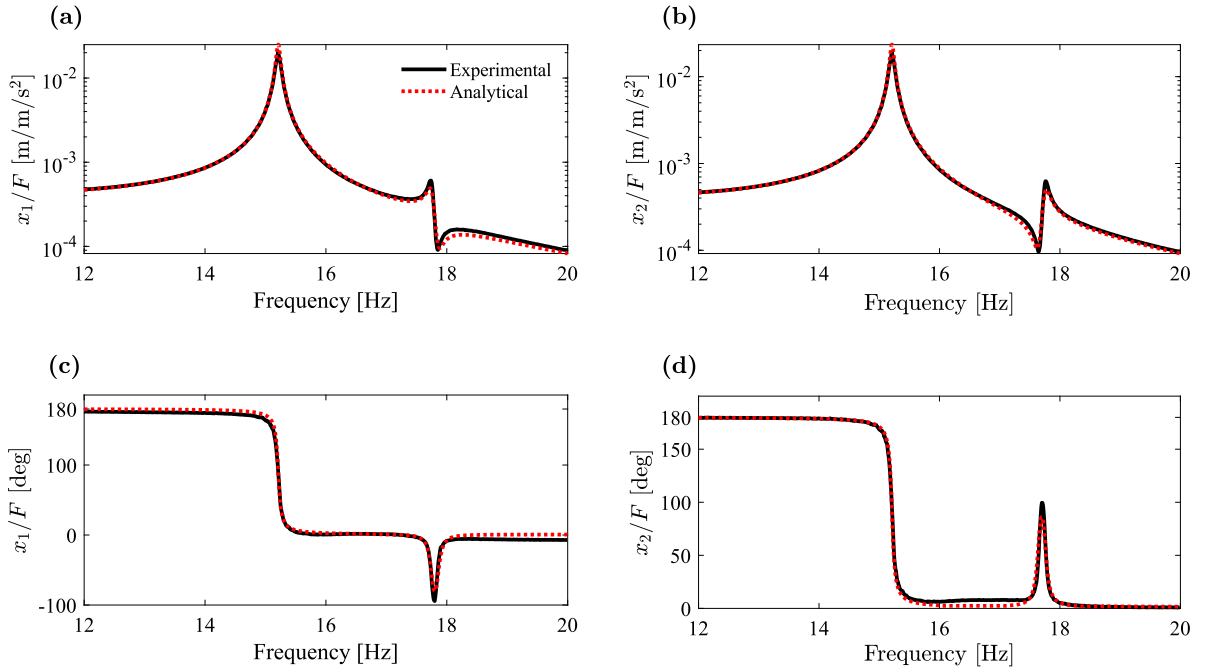
(a)

(b)

(c)

(d)

Fig. 7. Comparison between the experimental (black continuous line) and the analytical optimised (red dotted line) transfer functions. The transfer functions are plotted in terms of the amplitude (a–b) and the phase (c–d) for the two degrees of freedom.

in strategic locations (see Appendix B for a practical example). When this technique is impractical, dedicated methodologies for the estimation of modal mass are also available in the literature [58,60].

3.2. Nonlinear restoring force method: application to a ROM

Once the underlying linear behaviour is identified, it is possible to focus the attention on the nonlinear response of the system. The knowledge of the underlying linear system can be exploited to compute the nonlinear restoring force and the associated surfaces. The NLRF method can be applied by manipulating the general equation of motion of a n-DOF reduced-order mechanical system in matrix form, resulting in the following equation:

$$\mathbf{N}_{RF} = \mathbf{N}(\dot{\mathbf{x}}, \mathbf{x}) = \mathbf{F} - \mathbf{M}\ddot{\mathbf{x}} - \mathbf{C}\dot{\mathbf{x}} - \mathbf{K}\mathbf{x} \tag{6}$$

where $\mathbf{x} \in \mathbb{R}^{n \times 1}$ is the displacement vector, $\mathbf{M}$, $\mathbf{C}$, and $\mathbf{K} \in \mathbb{R}^{n \times n}$, represent the mass, damping, and stiffness matrices of the linear system, while $\mathbf{N}(\dot{\mathbf{x}}, \mathbf{x})$ and $\mathbf{F} \in \mathbb{R}^{n \times 1}$ are the nonlinear contribution and forcing function. Eq. (6) shows that the nonlinear restoring force $\mathbf{N}_{RF}$ represents the nonlinear contribution of the system which is exactly what the proposed method wants to identify. The method assumes that a previous identification of the underlying linear system has been performed, as shown in Section 3.1, thus the left-hand side of Eq. (6) is considered to be known for each measured time instant. This allows us to plot an NLRF surface for each degree of freedom. It is important to note two facts: firstly, the method needs to define a reduced-order model for its application. This limits the number of NLRF surfaces and the complexity of the subsequent identification process. Secondly, the method utilises physical coordinates. This decision is driven by the straightforward nature of these coordinates, which enables easy integration with experimental sensors and facilitates a clear understanding of the resulting surfaces in a physical context. Furthermore, in their study, Marsi et al. [49] highlighted that modal coordinates tend to converge faster than physical coordinates when dealing with high-order systems. However, the method proposed here is based on the adoption of ROMs, which significantly decreases the model order, effectively mitigating the convergence issue.

The nonlinear restoring force vector $\mathbf{N}_{RF}$ of Eq. (6) contains all the nonlinear terms that must be identified. Originally, the classical RFS method adopted Chebyshev series [43] for the identification process, but simple polynomial expansions have been demonstrated to be superior in terms of simplicity, accuracy, and speed of parameters estimation of the nonlinear contributions [40]. Nonetheless, one should be careful in the utilisation of such polynomials without prior knowledge of the system, as the restoring force may not be governed by integer-power polynomials (e.g., in the case of rubber, non-integer polynomials provide a good approximation of the nonlinear functional [61]) or could be accurately modelled by non-smooth functions. In this work, we have focused the attention on lightweight structures with geometric nonlinearities for which an integer-order polynomial is found to be a good approximation, as shown in other works [32,31,35]. This is also confirmed by prior successful identification of a similar nonlinear system [55], where a polynomial integer order is adopted. Considering different time instants, $\mathbf{N}_{RF}$ is matrix $n \times m$, where

n represents the number of reduced-DOF while m indicates the time instant at which the restoring force is measured. Mathematically, a least mean square problem can be formulated for each degree of freedom, as follows:

$$\mathbf{N}_{RF,n} = \mathbf{p}(\mathbf{x}, \dot{\mathbf{x}}, a_1, \ldots, a_k) = \mathbf{A}(\mathbf{x}, \dot{\mathbf{x}})\mathbf{b} \tag{7}$$

where $\mathbf{N}_{RF,n}$ is a vector with dimensions m $\times$ 1, which varies in time and represents the nonlinear restoring force of a single DOF, $\mathbf{p}$ is a vector representing the values of a polynomial which depends on the coefficients a_k and the displacement/velocities of each DOF, A is a squared matrix with dimensions $m \times k$, and $\mathbf{b} = [a_1, \ldots, a_k]$ is a vector $k \times 1$. By solving Eq. (7), it is possible to get an estimation of the coefficients contained in $\mathbf{b}$, which corresponds to the estimation outlined in phase II of Fig. 5. The coefficients obtained are then used as a starting point for a minimisation procedure which uses the following objective function $\mathbf{G}$:

$$\mathbf{G}(\mathbf{b}) = \mathbf{N}_{RF,n} - \mathbf{p}(\mathbf{x}, \dot{\mathbf{x}}, \mathbf{b}) \tag{8}$$

As for the linear identification procedure, the MATLAB minimisation function *lsqnonlin* is used to perform the numerical optimisation procedure. Now, by considering the ROM of Eq. (2), the nonlinear restoring force vector $\mathbf{N}_{RF}$ can be reduced to the following expression:

$$\mathbf{N}_{RF} = \begin{cases} N_{RF,1}(z_1, z_2, \dot{z}_1, \dot{z}_2) = -m\ddot{x}_1 - c_1\dot{z}_1 - c_2(\dot{z}_1 - \dot{z}_2) - k_1 z_1 - k_2(z_1 - z_2) \\ N_{RF,2}(z_1, z_2, \dot{z}_1, \dot{z}_2) = -m\ddot{x}_2 - c_3\dot{z}_2 + c_2(\dot{z}_1 - \dot{z}_2) - k_3 z_2 + k_2(z_1 - z_2) \end{cases} \tag{9}$$

Thus, the polynomial that we are seeking depends on the following general form:

$$p(z_1, z_2, \dot{z}_1, \dot{z}_2, a_1, \ldots, a_k) = a_1 z_1^2 + a_2 z_2^2 + a_3 \dot{z}_1^2 + a_4 \dot{z}_2^2 + a_5 z_1 z_2 + \cdots + a_{11} z_1^3 + a_{12} z_2^3 + a_{13} \dot{z}_1^3 + a_{14} \dot{z}_2^3 + \cdots \tag{10}$$

where k represents the number of coefficients and, having removed the linear contribution, the second degree is the lowest power in the polynomial expansion.

3.3. Nonlinear restoring force method: numerical example

A numerical example is now presented to illustrate the application of the NLRF method to a generic ROM. In particular, the numerical example wants to show how the NLRF surfaces are used to simplify the identification procedure, obtaining additional information on the nonlinear dynamics of the system. This enables engineering considerations that simplify the polynomial representation of the nonlinear restoring force. To provide parallelism with the considered experimental model, the MDOF nonlinear oscillator of Eq. (2) is considered in two different versions: the first version (case A) considers the presence of nonlinearities only between the support and the masses. The second one (case B), instead, considers a full nonlinear system. Table 5 resumes the property utilised in the two numerical examples and shows that only cubic stiffnesses are applied to the model. The equation of motion can be rewritten as:

$$m\ddot{z}_1 + c_1\dot{z}_1 + c_2(\dot{z}_1 - \dot{z}_2) + k_1 z_1 + k_2(z_1 - z_2) + \mu_1 z_1^3 + \mu_2(z_1 - z_2)^3 = -m\ddot{y} \tag{11a}$$

$$m\ddot{z}_2 + c_3\dot{z}_2 - c_2(\dot{z}_1 - \dot{z}_2) + k_3 z_2 - k_2(z_1 - z_2) + \mu_3 z_2^3 - \mu_2(z_1 - z_2)^3 = -m\ddot{y} \tag{11b}$$

The numerical data are obtained by solving Eq. (11) with the function *ode45*, a Runge–Kutta numerical integration scheme implemented in MATLAB. The data collection procedure emulates the procedure used to acquire the experimental data: a forward frequency sweep with a step of 0.16 Hz from 15.5 to 23.5 Hz is performed and the entire time histories of the two masses are saved in a vector form. Fig. 8 shows the absolute displacements of the two masses for case A. The figure displays the presence of two bent resonance peaks just after the natural frequencies of the system, which feature the typical jumping phenomena of nonlinear structures. Although nonlinearities are applied only on external elements, the time-history representation is not able to tell where the nonlinearities are applied to the system, as the jumps are present in both peaks of the two recorded signals. On the other hand, using the NLRF surfaces, it is possible to obtain additional information on the system dynamics. Fig. 9 represents the surfaces for the two considered numerical examples in two different reduced nonlinear spaces, i.e. z_1 and $\dot{z}_1$ for $N_{RF,1}$ and z_2 and $\dot{z}_2$ for $N_{RF,2}$. Panels (g–h) of Fig. 9 represent the NLRF surfaces associated with a full nonlinear system (case B). In this case, the NLRF surfaces are not a function in the considered 3D space, i.e., they are hyper-surfaces[2] as the nonlinear contribution on each mass depends on more than one mechanical DOF. This is clearly shown by the lateral views in the panels (e–f), where it is shown that for some elements of the nonlinear domain, there exists more than one value of the NLRF surface. Panels(c–d) and the associated lateral view of Fig. 9(a–b) show the NLRF surfaces of case A; they demonstrate that all the nonlinear orbits are laying on a surface that is graphically representable in a 3D space. This is possible because, in this case, the nonlinearities are localised only between the masses and the supports. Therefore, having eliminated the linear contributions of the restoring force, it is possible to obtain a unique relationship between the points of the nonlinear domain and the NLRF surface, hence we can represent the NLRF as a function in a 3D space. It is important to note that, given a mechanical MDOF system, the classical definition of the restoring force, with linear and nonlinear contributions, leads to a hyper-surface. This is logical, as the minimal mechanical MDOF system is characterised by two mechanical DOFs that possess two states each, a displacement and a velocity. Nonetheless, moving to a space dominated by only

---

[2] For hyper-surface it is intended a surface function that depends on a number of parameters larger than two, hence that is not representable as a function in a 3D space. On the contrary, surfaces are a function of two parameters which enables the representation in a 3D space.

Table 5

Linear and nonlinear parameters adopted in the numerical example.

Case	m [kg]	k_1 [N/m]	k_2 [N/m]	k_3 [N/m]	c_1 [Ns/m]	c_2 [Ns/m]	c_3 [Ns/m]	μ_1 [N/m³]	μ_2 [N/m³]	μ_3 [N/m³]	Y [mm]
A	1.0×10^{-1}	1.5×10^3	2.5×10^2	1.0×10^3	3.0×10^{-2}	2.5×10^{-2}	6.5×10^{-2}	5.0×10^6	0.0	2.8×10^6	5.0×10^{-2}
B	1.0×10^{-1}	1.5×10^3	2.5×10^2	1.0×10^3	3.0×10^{-2}	2.5×10^{-2}	6.5×10^{-2}	5.0×10^6	1.0×10^6	2.8×10^6	5.0×10^{-2}

Table 6

Nonlinear coefficients identified in the numerical test (case A). To improve the readability, the computer zero values are denoted by ∅. For each restoring force surface, a different polynomial is used.

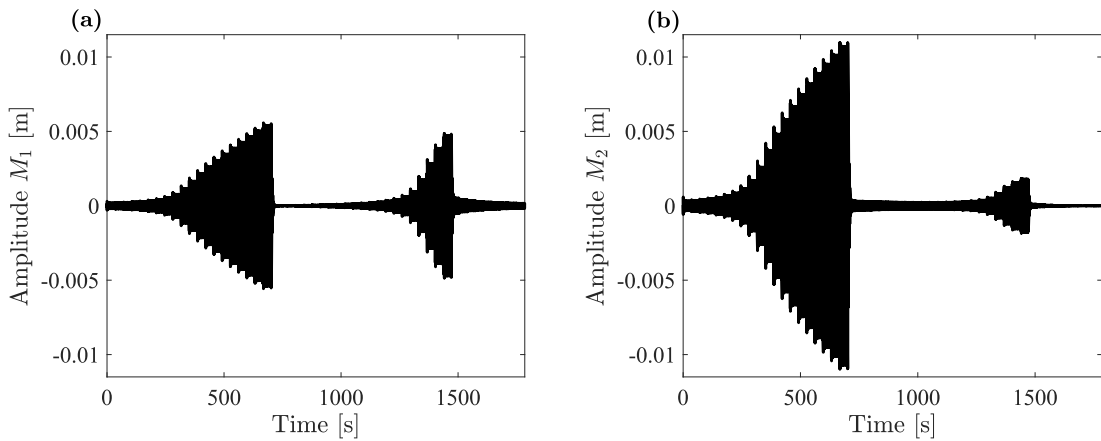| Monomial (M_1)	Coefficient	Value	Monomial (M_2)	Coefficient	Value
z_1^2	a_1	∅	z_2^2	b_1	∅
$z_1\dot{z}_1$	a_2	∅	$z_2\dot{z}_2$	b_2	∅
$\dot{z}_1^2$	a_3	∅	$\dot{z}_2^2$	b_3	∅
z_1^3	a_4	5.00×10^6 N/m³	z_2^3	b_4	2.80×10^6 N/m³
$\dot{z}_1^3$	a_5	∅	$\dot{z}_2^3$	b_5	∅
$z_1\dot{z}_1^2$	a_6	∅	$z_2\dot{z}_2^2$	b_6	∅
$z_1^2\dot{z}_1$	a_7	∅	$z_2^2\dot{z}_2$	b_7	∅

Fig. 8. Numerical time history of the first (a) and second (b) DOF. The numerical results are obtained with the reduced order model described by Eq. (11), using the parameters reported in Table 5 (only case A).

the nonlinear contribution of the restoring force, it is possible to represent the restoring force surfaces as a function in a 3D space if the above-mentioned conditions apply. This fact has important consequences for systems characterised by localised nonlinearities. In case A, it is possible to assume a simplified version of the polynomial which considers a single mechanical DOF, reducing Eq. (10) to the following:

$$\mathbf{N}_{RF} = \begin{cases} N_{RF,1}(z_1, \dot{z}_1) = a_1 z_1^2 + a_2 \dot{z}_1^2 + a_3 z_1 \dot{z}_1 + a_4 z_1^3 + a_5 \dot{z}_1^3 + a_6 z_1^2 \dot{z}_1 + \cdots \\ N_{RF,2}(z_2, \dot{z}_2) = b_1 z_2^2 + b_2 \dot{z}_2^2 + b_3 z_2 \dot{z}_2 + b_4 z_2^3 + b_5 \dot{z}_2^3 + b_6 z_2^2 \dot{z}_2 + \cdots \end{cases} \tag{12}$$

At this point, knowing the linear matrices, it is possible to identify the nonlinear contributions by using Eqs. (7) and (8). For the sake of simplicity, the identification is performed only for case A and the identified parameters are reported in Table 6 for a full third-order polynomial. The table shows that the nonlinear coefficients are correctly identified and the absence of noise allows reaching a perfect match between the assumed polynomials and the numerical data. The numerical test has served as a simple example to demonstrate how the method works and how the NLRF surfaces are used to simplify the assumed polynomials in a nonlinear ROM.

3.4. Experimental identification of the nonlinear system and model validation

The NLRF method is now employed to identify the nonlinear contribution of the experimental system depicted in Fig. 1. Although having a direct measure of the displacement, velocity, and acceleration for each measurement point would be ideal [62], numerical integration and differentiation procedures have been demonstrated to produce reliable RFS [45]. In this work, the accelerometer and vibrometer signals are integrated numerically, while the velocity of the vibrating table is obtained with numerical differentiation. The time data are then filtered with a high-pass filter (5 Hz) and a low-pass filter (75 Hz) to obtain smooth surfaces.

Based on the considered ROM, Eq. (9) can be used to obtain the experimental nonlinear restoring force by leveraging the knowledge of the system linear behaviour and the experimental measures. Like for the considered numerical cases, the first NLRF
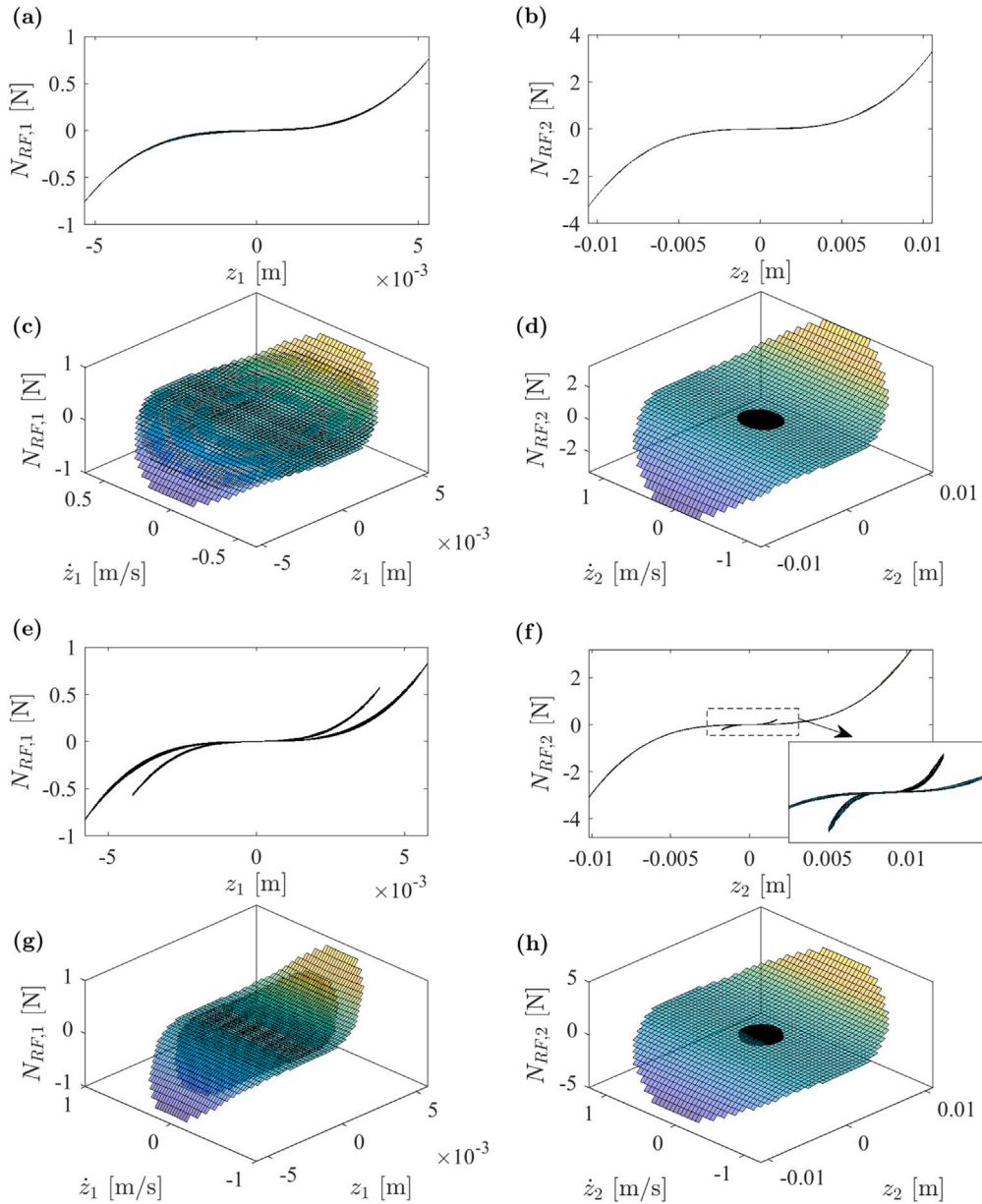
Fig. 9. Numerical nonlinear restoring force surfaces for case A ($\mu_1 = 5.0e6$ N/m^3, $\mu_2 = 0.0$ N/m^3, and $\mu_3 = 2.8e6$ N/m^3) (a–d) and case B ($\mu_1 = 5.0e6$ N/m^3, $\mu_2 = 1.0e6$ N/m^3 , and $\mu_3 = 2.8e6$ N/m^3) (e–h). Zooms in the plane relative displacement-nonlinear restoring force are reported for each diagram. The numerical results are obtained with the reduced order model described by Eq. (11) and the parameters reported in Table 5.

surface (Fig. 10(a)) is plotted in the space of the coordinates of the first mass, i.e. z_1 and $\dot{z}_1$ while the second one (Fig. 10(b)) is plotted in the space z_2 and $\dot{z}_2$. The figure demonstrates that, in those spaces, the restoring force surfaces generated by the nonlinear orbits, can be represented as a function in a 3D space. Thus, it is possible to deduce that the nonlinear behaviour of each mass can be fully described with only the local mechanical DOF, e.g., $N_{RF,1}$ is fully described by z_1 and $\dot{z}_1$. In other words, the external beams between the masses and the supports provide the majority of the nonlinear restoring contribution. This does not imply that beams in the between of the two masses have a pure linear behaviour, but that their nonlinear contribution is negligible, hence their nonlinearity is *inactivated*. The authors want to stress this aspect and highlight that this has important consequences on the identification of nonlinear structures, as inactivated nonlinearities can remain hidden until adequate excitation conditions are met. Nonetheless, a complete analysis of the effect of the forcing conditions on the identification process is out of the scope of this paper, therefore the experimental analysis and the subsequent validation will be limited to the excitation conditions described in Section 2.
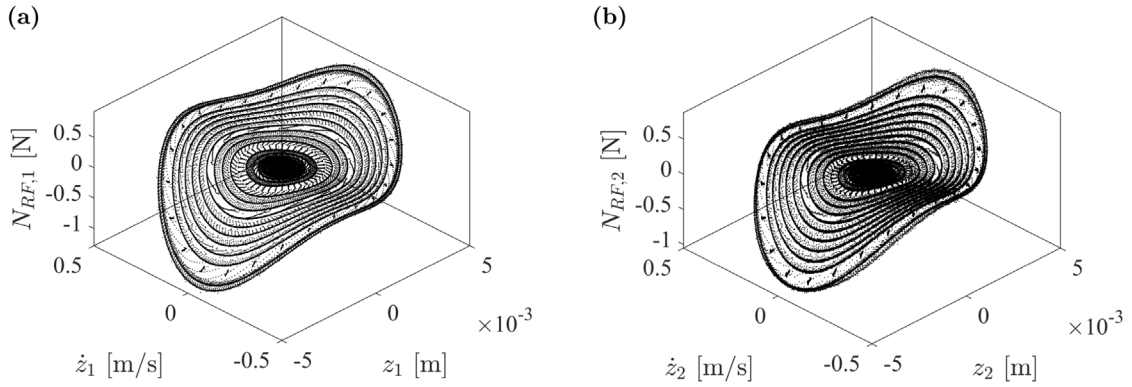
(a) **(b)**

Fig. 10. Experimental NLRF surfaces of the first (a) and second mass (b) obtained from the measurement: forward frequency sweep with excitation amplitude equal to 0.05 mm.
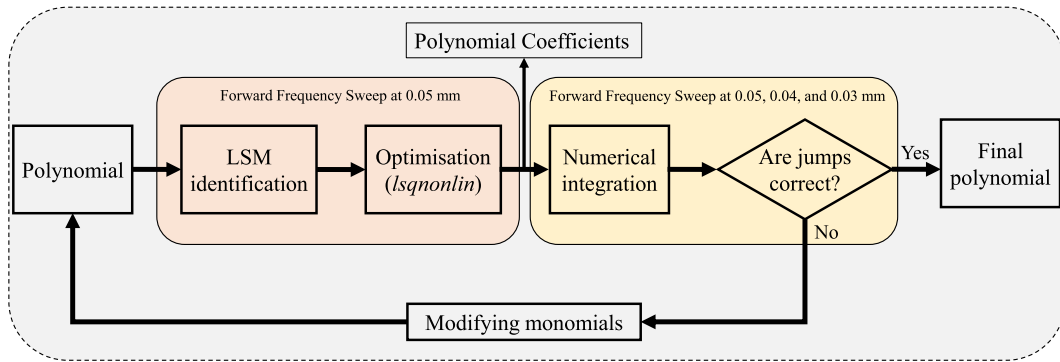

Fig. 11. Iterative procedure for the definition of the polynomial order. The identification of the polynomial coefficients is performed with one experimental data set, namely the forward frequency sweep at 0.05 mm of displacement amplitude, while the validation of the identified data is performed with three experimental data sets, i.e. the forward frequency sweep at 0.05, 0.04, and 0.03 mm of displacement amplitude.

Table 7
Experimental nonlinear coefficients, identified from the nonlinear restoring force surfaces. For each restoring force surface, i.e. for each degree of freedom, a different polynomial is adopted as prescribed in the table. For graphical representation, unused lines are denoted by −.

Monomial (M_1)	Coefficient	Value	Monomial (M_2)	Coefficient	Value
z_1^2	a_1	-8.4608×10^3 N/m^2	z_2^2	b_1	-8.3989×10^3 N/m^2
$z_1 \dot{z}_1$	a_2	5.3189 Ns/m^2	$z_2 \dot{z}_2$	b_2	-4.8546 Ns/m^2
$\dot{z}_1^2$	a_3	0.9055 Ns^2/m^2	$\dot{z}_2^2$	b_3	0.9047 Ns^2/m^2
z_1^3	a_4	1.1237×10^7 N/m^3	z_2^3	b_4	1.1231×10^7 N/m^3
$\dot{z}_1^3$	a_5	1.9777 Ns^3/m^3	$\dot{z}_2^5$	b_5	-8.0214 Ns^5/m^5
$z_1 \dot{z}_1^2$	a_6	-1.3876×10^2 Ns^2/m^3	−	−	−
$z_1^2 \dot{z}_1$	a_7	1.0495×10^4 Ns/m^3	−	−	−

   In order to validate the model, only one experimental FRC is used to create the nonlinear restoring force surface and to identify the polynomial. To this end, the measurement conducted at a base amplitude equal to 0.05 mm is adopted in the identification process, while the model prediction capabilities are tested against the experimental measurements obtained with different excitation amplitudes, namely 0.04 and 0.03 mm.

   Different polynomials are tested to identify the experimental nonlinear restoring force surfaces correctly: as the classical restoring force surface method for MDOF systems [49], the proposed method suffers from the exponential increase of unknowns. Indeed, by increasing the dimension of the polynomial, i.e., the number of variables and maximum order, the number of unknowns increases exponentially, leading to computationally expensive calculations. By using the proposed method, the number of variables for each polynomial can be considerably reduced by exploiting the evidence provided by the experimental data, i.e., by the NLRF surfaces of Fig. 10(a–b), which, as explained, suggest the presence of localised nonlinearities between the two masses and the external supports. This permits the use of two sets of variables, namely z_1, $\dot{z}_1$ for the first surface and z_2, and $\dot{z}_2$ for the second one, enabling the usage of Eq. (12) to represent the nonlinear polynomials. The polynomial order, instead, is chosen with the iterative procedure
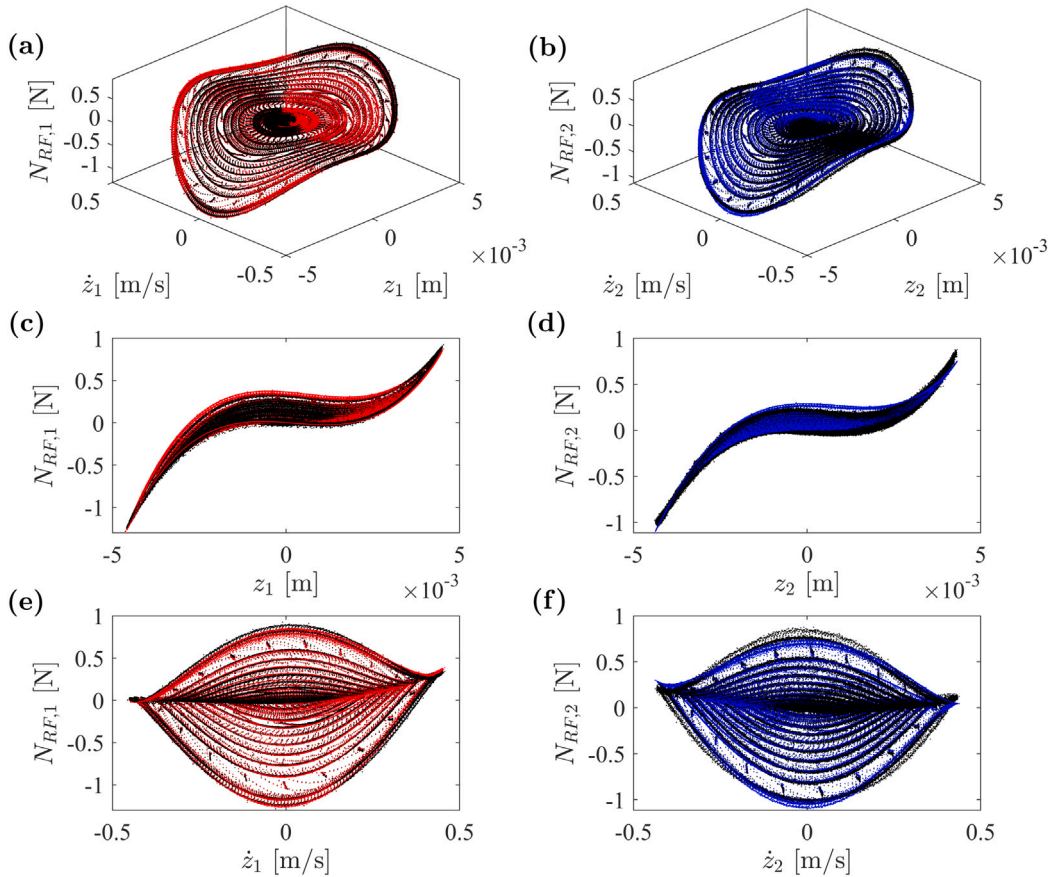
Fig. 12. Comparison between the identified (red and blue) and the experimental (black) nonlinear restoring force surfaces. The experimental data are obtained from the forward frequency sweep with excitation amplitude equal to 0.05 mm. The left panels describe the NLRF surfaces of the first mass (a, c, e), while the right panels illustrate the surfaces associated with the second mass (b, d, f). Different views are reported: panels (a) and (b) report the isometric view, panels (c) and (d) illustrate the lateral view, and panels (e) and (f) show the frontal view.
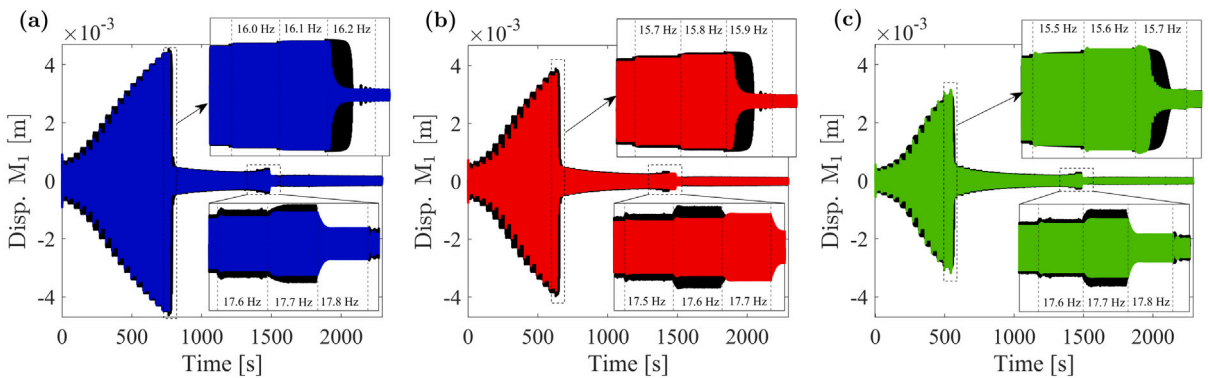

Fig. 13. Time histories comparison between the experimental data (black line) and the numerical results (coloured lines) for excitation amplitudes equal to: 0.05 (a) (blue line), 0.04 mm (b) (red line), and 0.03 mm (c) (green line). Zooms in correspondence of the first and second resonance are reported for each case.

schematically reported in Fig. 5 and proposed in Fig. 11 with additional details: firstly a polynomial is assumed, then the associated coefficients are identified with an LMS and optimisation procedures, and finally, the numerical predictions of the identified model are compared against sets of experimental data that are different from the one adopted in the identification process. In detail, the

polynomial coefficients are identified by using the experimental restoring force generated with an excitation amplitude of 0.05 mm, while the validation is performed against the experimental time histories measured at the excitation amplitudes of 0.03, 0.04, and 0.05 mm. The numerical time histories are generated via numerical integration procedures by using perfect sinusoidal excitation and the MATLAB function *ode45* and the same discrete frequency sweep adopted in the experimental measurements. This allows to discover at which frequency the jumps occur in the three different numerical simulations. If the jumps occur at the same frequency as the associated experimental data then the polynomial can be considered validated. Otherwise, the polynomial is modified by increasing the order and removing each monomial with a low contribution, until the correct jumps are identified. It should be noted that the usage of ideal sinusoidal excitation and a ROM allows for performing inexpensive numerical simulations and testing many different polynomials in a short time.

The final results are reported in Table 7: it is clear that the first polynomial is correctly identified with a full polynomial of order 3. Instead, the polynomial associated with the second surface needs some changes: in particular the third-order mixed terms and the third-order damping terms do not allow to achieve correct jumps in the numerical simulations. Thus, following the aforementioned iterative procedure, they are removed and substituted with a fifth-order damping term. Fig. 12 shows the comparison between numerical and experimental NLRF surfaces for the two DOFs. Different views are proposed with the left and right panels showing, respectively, the surface associated with the first and second mass. The numerical and experimental data exhibit a good match, providing the necessary accuracy to the selected polynomial. Fig. 13 shows the comparison between the numerical and the experimental time histories for the first mass at the three different levels of excitation, i.e., 0.05 mm (Fig. 13(a)), 0.04 mm (Fig. 13(b)), and 0.03 mm (Fig. 13(c)). Overall, there is a very good match between the numerical and experimental dynamic responses at all the considered excitation levels, in terms of amplitude and frequency at which the jumps occur. To show the good prediction capabilities of the identified model, zooms are reported in Fig. 13 near the resonances. The passage from high- to low-amplitude of response in the second resonance peak (around 17.5–17.8 Hz) is perfectly caught by the numerical model. On the contrary, very small discrepancies between the experimental data and numerical predictions are found at the first jump, with the numerical jump occurring prematurely. This is due to the experimental control system which needs time to move from high- to low-amplitude response. Such a delay is not accounted for in the numerical simulations, leading to premature jumps.

In order to fully validate the identified model, the experimental and numerical nonlinear FRCs are compared. The displacement amplitude is selected for comparison because the experimental restoring force surfaces indicate the hardening stiffness characteristics as the predominant nonlinear behaviour. The numerical FRCs are computed with numerical continuation procedures at the three different levels of excitation. These procedures allow the continuation of limit cycles with respect to one or more parameters [63,64]; thus, the FRCs are obtained by continuing stable orbits with respect to the excitation frequency Ω. Different numerical continuation toolboxes are available in the literature; in this work, the toolbox *COCO* [65] is used to compute the complete FRCs of the identified system. In order to perform the numerical continuation, the following autonomous version of the identified ROM is used:

$$\dot{z}_1 = w_1 \tag{13a}$$

$$\dot{w}_1 = -\frac{c_1}{m}w_1 - \frac{k_1}{m}z_1 - \frac{c_2}{m}(w_1 - w_2) - \frac{k_2}{m}(z_1 - z_2) - \frac{1}{m}N_{RF,1} - \ddot{Y}u \tag{13b}$$

$$\dot{z}_2 = w_2 \tag{13c}$$

$$\dot{w}_2 = -\frac{c_3}{m}w_2 - \frac{k_3}{m}z_2 + \frac{c_2}{m}(w_1 - w_2) + \frac{k_2}{m}(z_1 - z_2) - \frac{1}{m}N_{RF,2} - \ddot{Y}u \tag{13d}$$

$$\dot{u} = -\Omega v + u(1 - u^2 - v^2) \tag{13e}$$

$$\dot{v} = \Omega u + v(1 - u^2 - v^2) \tag{13f}$$

where u, v, and w are additional states that are necessary to reach a first-order autonomous formulation of the system. It should be noted that the acceleration amplitude $\ddot{Y}$ can be computed from the measured displacement amplitude Y with the following expression: $\ddot{Y} = -\Omega^2 Y$. The nonlinear terms $N_{RF,1}$ and $N_{RF,2}$, instead, are obtained from the previous identification process and precisely are:

$$\begin{cases} N_{RF,1} = a_1 z_1^2 + a_2 z_1 w_1 + a_3 w_1^2 + a_4 z_1^3 + a_5 w_1^3 + a_6 z_1 w_1^2 + a_7 z_1^2 w_1; \\ N_{RF,2} = b_1 z_2^2 + b_2 z_2 w_2 + b_3 w_2^2 + b_4 z_2^3 + b_5 w_2^5; \end{cases} \tag{14}$$

where the coefficients a and b can be found in Table 7. Fig. 14 shows the comparison between the FRCs: the panels in each row represent the comparison between numerical and experimental FRCs obtained with a certain excitation amplitude, equal to 0.05 mm (upper row), 0.04 mm (middle row), and 0.03 mm (lower row). The columns, instead, divide the FRCs associated with the first mass (left panels) and the second mass (right panels). All the numerical simulations are in good agreement with the experimental data: in particular, the identified model is able to reproduce with a good level of accuracy the FRCs of the two masses at all the considered excitation levels. Moreover, the model effectively scales the amplitude of the response and the jumps in accordance with the varying levels of excitation. The good match between numerical and experimental FRCs demonstrates that the chosen ROM is able to correctly catch the complex nonlinear behaviour of the experimental test rig, characterised by the presence of stiffness and damping nonlinear properties. It is worth noting that the considered experimental system incorporates quasi-real interfaces, i.e., it has complex interfaces between the different components; this introduces additional complexities in the dynamic response at large amplitude, e.g., friction, imperfect symmetries, imperfect clamping, and contacts. Nonetheless, it is demonstrated that a simplified ROM with two DOFs can describe its full dynamics, even when large displacements are achieved.
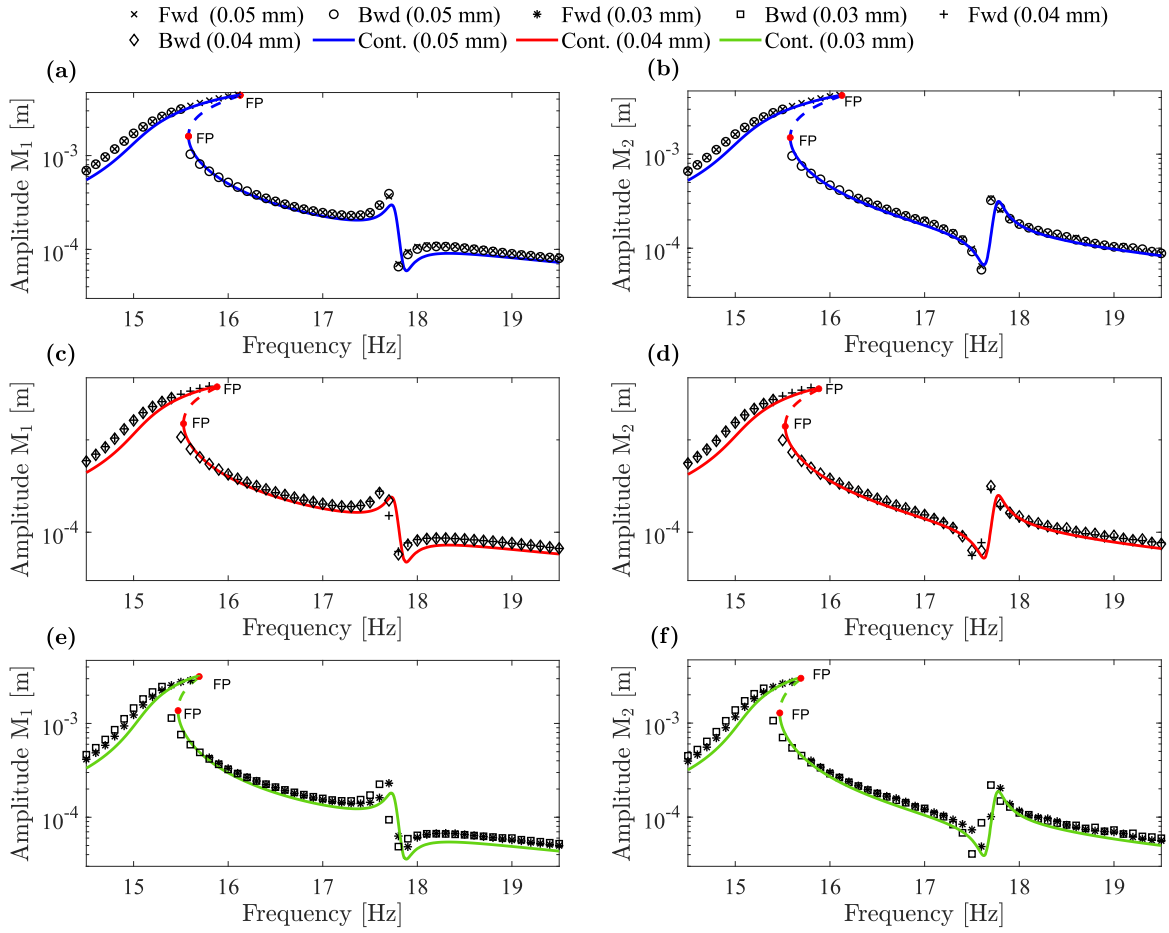
Fig. 14. Comparison between the numerically continued (coloured continuous line) and experimental (black markers) FRCs. The numerical FRCs are obtained from the identified ROM and the results are compared with the experiments for input amplitude equal to: 0.05 mm (a–b), 0.04 mm (c–d), and 0.03 mm (e–f). The left panels describe the FRCs associated with the displacement of the first mass (a, c, e), while the right panels illustrate the FRCs obtained from the second mass displacement (b, d, f). FP prescribes the presence of a fold point.

Fig. 15 shows the numerical FRCs in the same plot for the first (left panel) and second mass (right panel). The first peak reaches larger response amplitudes, showing the typical saturation effect and the presence of unstable solutions (dashed line) in all three levels of excitation. The second peak, instead, remains in the linear regime mostly, therefore, no unstable solutions are found. The zooms of the first peak show the presence of fold points, which define where the limit cycles change their stability, passing from stable to unstable and vice versa. The middle grey continuous line prescribes the backbone curve which represents the undamped unforced dynamic response of the system in the frequency-amplitude plot. The continuation of the conservative periodic solutions can be achieved as suggested by Doedel et al. [66,54] and the full derivation of the modified equations of motion with the unfolding parameter is reported in the Appendix A. Both the backbone curves have a hardening effect, bending towards higher frequencies when large amplitudes of responses are reached. Therefore they have the expected behaviour, confirming the correctness of the identified model. Finally, thanks to the presence of only trivially resonant terms,[3] no bifurcation points or flipping solutions are found in the backbones curves which testifies to the absence of internal resonances in the considered range of amplitude of response.

4. Conclusion

This study presented a novel procedure for the identification of MDOF-ROMs representing lightweight structures featuring large deformations. The proposed method, named the NLRF method, wants to pave the way towards more systematic use of nonlinear

---

[3] For a formal definition of resonant, trivially resonant, and non-resonant terms, the interested reader should refer to [17].
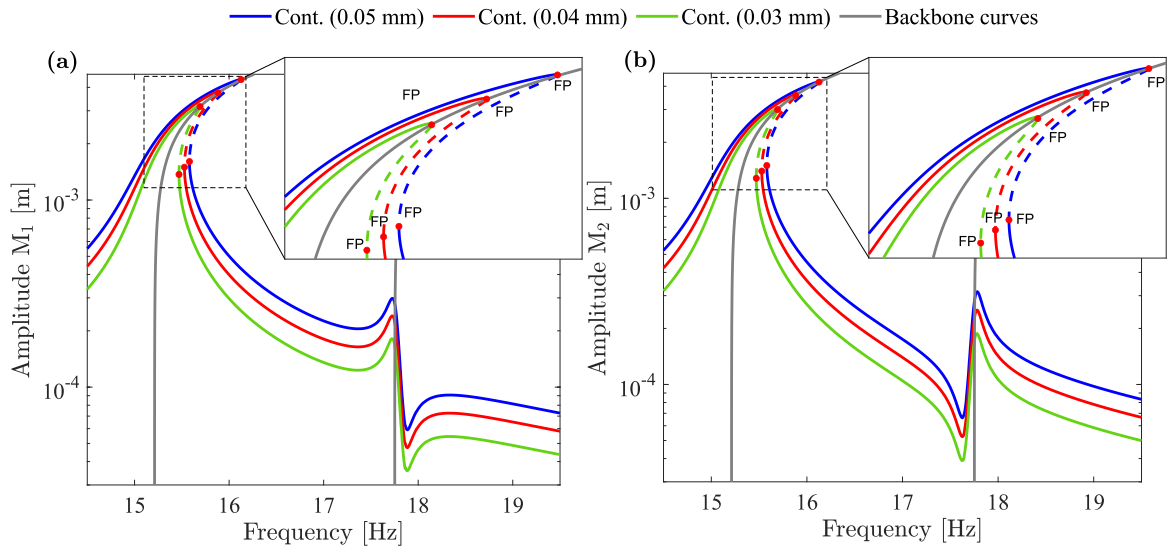
Fig. 15. Frequency response curves obtained from the numerical continuation of the identified model, in terms of displacement of first (a) and second (b) mass. The frequency response is reported for different excitation amplitudes, namely 0.03 mm (green line), 0.04 mm (red line), and 0.05 mm (blue line). Backbone curves (grey line) are shown for the two considered modes.

dynamic models in the identification procedures adopted in industry. To this end, the NLRF method is built on existing identification methods and is based on separating the restoring force in linear and nonlinear components. Thanks to this separation, the representation of the nonlinear restoring force surface is shown to exist in a reduced sub-space when the nonlinearities are localised in a single portion of the system. This results in a simplified modelisation of the associated ROM, whose nonlinear contributions can be described in a reduced form. More importantly, the proposed method represents a natural extension of the current identification practices in the industrial environment as the identification of the nonlinear contributions is considered as a second stage after the identification of the linear behaviour of the system. To validate the identified MDOF-ROM, a lightweight structure featuring lumped masses and elastic nonlinear connections is experimentally investigated. Numerical time histories and FRCs are compared with experimental measurements obtained from forward/backward frequency sweeps. In particular, the validation is performed against sets of experimental data obtained at excitation conditions different from the one used during the identification process. The results show a good match between the numerical and experimental data at all the considered excitation levels in terms of both amplitude and jumps, showing the effectiveness of the proposed identification procedure and demonstrating that MDOF-ROMs can correctly catch the complex dynamics of lightweight structures in nonlinear regimes.

CRediT authorship contribution statement

Cristiano Martinelli: Conceptualization, Data curation, Investigation, Methodology, Software, Validation, Visualization, Writing – original draft, Writing – review & editing. **Andrea Coraddu:** Conceptualization, Funding acquisition, Methodology, Project administration, Resources, Supervision, Writing – review & editing. **Andrea Cammarano:** Conceptualization, Supervision, Writing – review & editing.

Declaration of competing interest

The authors declare that they have no known competing financial interests or personal relationships that could have appeared to influence the work reported in this paper.

Data availability

The experimental data are available at the following DOI [66].
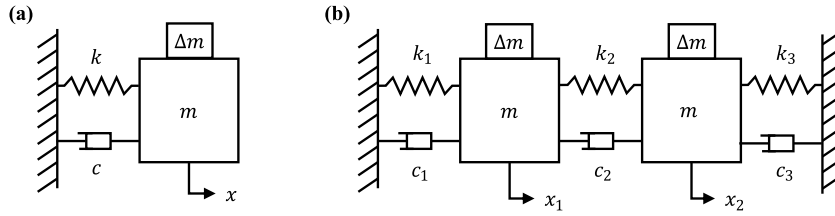
Acknowledgements

Fig. 16. SDOF (a) and MDOF (b) models utilised in the outlined mass estimation procedure.

Appendix A

In order to study the conservative behaviour of the system, the excitation and damping terms are removed from the equation of motion. The following expression represents the undamped unforced behaviour of the ROM:

$$\dot{z}_1 = w_1 \tag{15a}$$

$$\dot{w}_1 = -\frac{k_1}{m}z_1 - \frac{k_2}{m}(z_1 - z_2) - \frac{1}{m}N_{RF,1}(z_1) \tag{15b}$$

$$\dot{z}_2 = w_2 \tag{15c}$$

$$\dot{w}_2 = -\frac{k_3}{m}z_2 + \frac{k_2}{m}(z_1 - z_2) - \frac{1}{m}N_{RF,2}(z_2) \tag{15d}$$

where $N_{RF,1}(z_1)$ and $N_{RF,2}(z_2)$ denote the nonlinear restoring forces purified by the nonlinear damping terms. In particular, these terms can be expressed as follows:

$$\begin{cases} N_{RF,1} = a_1 z_1^2 + a_4 z_1^3; \\ N_{RF,2} = b_1 z_2^2 + b_4 z_2^3; \end{cases} \tag{16}$$

The calculation of the conserved mechanical energy is straightforward with the kinetic E_k and potential E_p energy denoted by:

$$E_k = \frac{1}{2}w_1^2 + \frac{1}{2}w_2^2 \tag{17a}$$

$$E_p = \frac{1}{2}\frac{k_1}{m}z_1^2 + \frac{1}{3}\frac{a_1}{m}z_1^3 + \frac{1}{4}\frac{a_4}{m}z_1^4 + \frac{1}{2}\frac{k_3}{m}z_2^2 + \frac{1}{3}\frac{b_1}{m}z_2^3 + \frac{1}{4}\frac{b_4}{m}z_2^4 + \frac{1}{2}\frac{k_2}{m}(z_1 - z_2)^2 \tag{17b}$$

Following the procedure outlined in Ref. [66] it is possible to continue periodic orbits of conservative systems by introducing the *unfolding* parameter λ. A term λw is added to the system, in Eqs. (15b) and (15c), to allow the continuation procedure. Then, a fixed point of the system, i.e. an equilibrium position at zero velocity and zero displacements, is continued with respect to the unfolding parameter which is initialised with a negative value. At $\lambda = 0$ a Hopf bifurcation of the system is found; this bifurcation generates the periodic oscillations of the conservative system which can be continued with respect to unfolding parameter λ. It is worth noting that the introduced parameter λ represents a damping element which is kept null during the whole continuation procedure. Nonetheless, to reduce the numerical oscillation of the unfolding parameter is possible to introduce the additional stabilising terms as suggested in Ref. [66]:

$$\dot{z}_1 = w_1 + \lambda\frac{\partial E}{\partial z_1} \tag{18a}$$

$$\dot{w}_1 = -\frac{k_1}{m}z_1 - \frac{k_2}{m}(z_1 - z_2) - \frac{a_1}{m}z_1^2 - \frac{a_4}{m}z_1^3 + \lambda\frac{\partial E}{\partial w_1} \tag{18b}$$

$$\dot{z}_2 = w_2 + \lambda\frac{\partial E}{\partial z_2} \tag{18c}$$

$$\dot{w}_2 = -\frac{k_3}{m}z_2 + \frac{k_2}{m}(z_1 - z_2) - \frac{b_1}{m}z_2^2 - \frac{b_4}{m}z_2^3 + \lambda\frac{\partial E}{\partial w_2} \tag{18d}$$

where $E = E_k + E_p$ represents the total conserved energy. By computing the partial derivatives, Eq. (18) can be transformed into the final set of equations which is used to compute the backbone curves.

Appendix B

The mass of a mechanical oscillator can be estimated by measuring the change in natural frequencies induced by adding known mass to the system, as schematically shown in Fig. 16. For example, in the case of an SDOF system, the natural frequency is $\omega_n = \sqrt{k/m}$. If $\omega_n^* = \sqrt{k/(m + \Delta m)}$ represents the natural frequency when an additional mass Δm is applied to the system, the original mass m of the system can be evaluated by knowing Δm, ω_n, and ω_n^*:

$$m = \frac{\Delta m\,\omega_n^{*2}}{\omega_n^2 - \omega_n^{*2}} \tag{19}$$

This expression is derived by imposing that the stiffness k of the oscillator does not change when the additional mass is considered. Experimentally, the natural frequencies ω_n and ω_n^* can be estimated using experimental modal analysis techniques and the added mass Δm can be directly measured. The outlined procedure is also applicable to the MDOF system investigated in this paper. In this case, two additional masses Δm should be applied to the system as shown in Fig. 16 (b). The squared natural frequencies of the system are:

$$\omega_{n,1}^2 = \frac{k_1 + 2k_2 + k_3 - \sqrt{k_1^2 - 2k_1 k_3 + 4k_2^2 + k_3^2}}{2m} \tag{20a}$$

$$\omega_{n,2}^2 = \frac{k_1 + 2k_2 + k_3 + \sqrt{k_1^2 - 2k_1 k_3 + 4k_2^2 + k_3^2}}{2m} \tag{20b}$$

The sum of the squared natural frequencies becomes $\omega_{n,1}^2 + \omega_{n,2}^2 = (k_1 + 2k_2 + k_3)/m$ and it can be expressed in the same form as an SDOF system, i.e. as $\omega_{eq}^2 = k_{eq}/m$. Thus, m can be identified using the following expression:

$$m = \frac{\Delta m \omega_{eq}^{*\,2}}{\omega_{eq}^2 - \omega_{eq}^{*\,2}} \tag{21}$$

Using numerical procedures, this approach can be extended to the case when the values of the masses are different.

References

[1] F.A. Prince, Weight and the future of space flight hardware cost modeling, in: International Society of Parametric Analysis/Society of Cost Estimating and Analysis 2003 International Conference, 2003.

[2] P. Fortescue, G. Swinerd, J. Stark, Spacecraft Systems Engineering, John Wiley & Sons, 2011.

[3] R.N. Yancey, Challenges, opportunities, and perspectives on lightweight composite structures: Aerospace versus automotive, Elsevier Inc., 2016, pp. 35–52, http://dx.doi.org/10.1016/B978-1-78242-325-6.00002-5,

[4] Department of Energy & Climate Change, The UK Low Carbon Transition Plan, Government of the United Kingdom, 2009.

[5] Official Journal of the European Union, The European Green Deal, European Parliament, 2020.

[6] Vehicles Technologies Office, FY 2014 Annual Progress Report - Lightweight Material R&D, US Department of Energy, 2014.

[7] P. Brøndsted, R.P.L. Nijssen, S. Goutianos, Advances in Wind Turbine Blade Design and Materials, Woodhead Publishing, 2023.

[8] K. Carney, I. Yunis, K. Smith, C.-Y. Peng, Nonlinear dynamic behavior in the cassini spacecraft modal survey, in: Proceedings of the 15th InternationalModal Analysis Conference, IMAC, Orlando, Florida, 1997, pp. 811–817.

[9] J.R. Ahlquist, J.M. Carreño, H. Climent, R. de Diego, J. de Alba, Assessment of nonlinear structural response in A400m GVT, in: Structural Dynamics, Volume 3: Proceedings of the 28th IMAC, a Conference on Structural Dynamics, 2010, Springer, 2011, pp. 1147–1155.

[10] G. Kerschen, M. Peeters, J.C. Golinval, C. Stéphan, Nonlinear modal analysis of a full-scale aircraft, J. Aircr. 50 (2013) 1409–1419, http://dx.doi.org/10.2514/1.C031918.

[11] H.H. Mian, G. Wang, Z.Y. Ye, Numerical investigation of structural geometric nonlinearity effect in high-aspect-ratio wing using CFD/CSD coupled approach, J. Fluids Struct. 49 (2014) 186–201, http://dx.doi.org/10.1016/j.jfluidstructs.2014.04.011.

[12] A. Martin, F. Thouverez, Dynamic analysis and reduction of a cyclic symmetric system subjected to geometric nonlinearities, J. Eng. Gas Turbines Power 141 (2019) http://dx.doi.org/10.1115/1.4041001.

[13] M.J. Patil, D.H. Hodges, On the importance of aerodynamic and structural geometrical nonlinearities in aeroelastic behavior of high-aspect-ratio wings, J. Fluids Struct. 19 (2004) 905–915, http://dx.doi.org/10.1016/j.jfluidstructs.2004.04.012.

[14] S. Quaegebeur, B. Chouvion, F. Thouverez, L. Berthe, Energy transfer between nodal diameters of cyclic symmetric structures exhibiting polynomial nonlinearities: Cyclic condition and analysis, Mech. Syst. Signal Process. 139 (2020) http://dx.doi.org/10.1016/j.ymssp.2019.106604.

[15] A. Vizzaccaro, Y. Shen, L. Salles, J. Blahoš, C. Touzé, Direct computation of nonlinear mapping via normal form for reduced-order models of finite element nonlinear structures, Comput. Methods Appl. Mech. Engrg. 384 (2021) http://dx.doi.org/10.1016/j.cma.2021.113957.

[16] Y. Shen, N. Béreux, A. Frangi, C. Touzé, Reduced order models for geometrically nonlinear structures: Assessment of implicit condensation in comparison with invariant manifold approach, Eur. J. Mech. A Solids 86 (2021) http://dx.doi.org/10.1016/j.euromechsol.2020.104165.

[17] C. Touzé, A. Vizzaccaro, O. Thomas, Model order reduction methods for geometrically nonlinear structures: A review of nonlinear techniques, Nonlinear Dynam. 105 (2021) 1141–1190, http://dx.doi.org/10.1007/s11071-021-06693-9.

[18] S. Shaw, C. Pierre, Non-linear normal modes and invariant manifolds non-linear normal modes and invariant manifolds non-linear normal modes and invariant manifolds, J. Sound Vib. 150 (1991) 170–173, http://dx.doi.org/10.1016/0022-460X(91)90412-D\"\i, URL https://hal.science/hal-01310674.

[19] S.W. Shaw, C. Pierre, Normal modes for non-linear vibratory systems, J. Sound Vib. 164 (1993) 85–124.

[20] S.W. Shaw, C. Pierre, Normal modes of vibration for non-linear continuous systems, J. Sound Vib. 169 (1994) 319–347.

[21] A.L. Kelley, Analytic two-dimensional subcenter manifold for system with an integral, Pacific J. Math. 29 (1969).

[22] A. Lyapunov, Problème général de la stabilité du mouvement, Ann. Fac. Sci. Toulouse Math. 9 (1907) 203–474.

[23] G. Haller, S. Ponsioen, Nonlinear normal modes and spectral submanifolds: Existence, uniqueness and use in model reduction, Nonlinear Dynam. 86 (2016) 1493–1534, http://dx.doi.org/10.1007/s11071-016-2974-z.

[24] C. Touzé, A Normal Form Approach for Nonlinear Normal Modes (Ph.D. thesis), LMA, 2003.

[25] C. Touzé, O. Thomas, A. Chaigne, Hardening/softening behaviour in non-linear oscillations of structural systems using non-linear normal modes, J. Sound Vib. 273 (2004) 77–101, http://dx.doi.org/10.1016/j.jsv.2003.04.005.

[26] E. Pesheck, N. Boivin, C. Pierre, S.W. Shaw, Nonlinear modal analysis of structural systems using multi-mode invariant manifolds, Nonlinear Dynam. 25 (2001) 183–205.

[27] M. McEwan, A Combined Modal / Finite Element Technique for the Non-Linear Dynamic Simulation of Aerospace Structures (Ph.D. thesis), The University of Manchester, 2001.

[28] A.A. Muravyov, S.A. Rizzi, Determination of nonlinear stiffness with application to random vibration of geometrically nonlinear structures, Comput. Struct. 81 (2003) 1513–1523, http://dx.doi.org/10.1016/S0045-7949(03)00145-7.

[29] M.P. Mignolet, C. Soize, Stochastic reduced order models for uncertain geometrically nonlinear dynamical systems, Comput. Methods Appl. Mech. Engrg. 197 (2008) 3951–3963, http://dx.doi.org/10.1016/j.cma.2008.03.032.

[30] J.P. Noël, L. Renson, C. Grappasonni, G. Kerschen, Identification of nonlinear normal modes of engineering structures under broadband forcing, Mech. Syst. Signal Process. 74 (2016) 95–110, http://dx.doi.org/10.1016/j.ymssp.2015.04.016.

[31] V. Denis, M. Jossic, C. Giraud-Audine, B. Chomette, A. Renault, O. Thomas, Identification of nonlinear modes using phase-locked-loop experimental continuation and normal form, Mech. Syst. Signal Process. 106 (2018) 430–452, http://dx.doi.org/10.1016/j.ymssp.2018.01.014.

[32] M. Jossic, O. Thomas, V. Denis, B. Chomette, A. Mamou-Mani, D. Roze, Effects of internal resonances in the pitch glide of Chinese gongs, J. Acoust. Soc. Am. 144 (2018) 431–442, http://dx.doi.org/10.1121/1.5038114.

[33] J.P. Noël, G. Kerschen, Frequency-domain subspace identification for nonlinear mechanical systems, Mech. Syst. Signal Process. 40 (2013) 701–717, http://dx.doi.org/10.1016/j.ymssp.2013.06.034.

[34] D.A. Czaplewski, S. Strachan, O. Shoshani, S.W. Shaw, D. López, Bifurcation diagram and dynamic response of a MEMS resonator with a 1:3 internal resonance, Appl. Phys. Lett. 114 (2019) http://dx.doi.org/10.1063/1.5099459.

[35] A. Givois, J.J. Tan, C. Touzé, O. Thomas, Backbone curves of coupled cubic oscillators in one-to-one internal resonance: Bifurcation scenario, measurements and parameter identification, Meccanica 55 (2020) 481–503, http://dx.doi.org/10.1007/s11012-020-01132-2.

[36] A. Givois, C. Giraud-Audine, J.F. Deü, O. Thomas, Experimental analysis of nonlinear resonances in piezoelectric plates with geometric nonlinearities, Nonlinear Dynam. 102 (2020) 1451–1462, http://dx.doi.org/10.1007/s11071-020-05997-6.

[37] M. Monteil, O. Thomas, C. Touzé, Identification of mode couplings in nonlinear vibrations of the steelpan, Appl. Acoust. 89 (2015) 1–15, http://dx.doi.org/10.1016/j.apacoust.2014.08.008.

[38] C. Martinelli, A. Coraddu, A. Cammarano, Approximating piecewise nonlinearities in dynamic systems with sigmoid functions: Advantages and limitations, Nonlinear Dynam. (2023) http://dx.doi.org/10.1007/s11071-023-08293-1.

[39] Y.S. Lee, G. Kerschen, A.F. Vakakis, P. Panagopoulos, L. Bergman, D.M. McFarland, Complicated dynamics of a linear oscillator with a light, essentially nonlinear attachment, Physica D 204 (2005) 41–69, http://dx.doi.org/10.1016/j.physd.2005.03.014.

[40] G. Kerschen, K. Worden, A. Vakakis, J.C. Golinval, Past, present and future of nonlinear system identification in structural dynamics, Mech. Syst. Signal Process. 20 (2006) 505–592.

[41] T.L. Hill, A. Cammarano, S.A. Neild, D.A.W. Barton, Identifying the significance of nonlinear normal modes, Proc. R. Soc. Lond. Ser. A Math. Phys. Eng. Sci. 473 (2017) http://dx.doi.org/10.1098/rspa.2016.0789.

[42] J.P. Noël, G. Kerschen, Nonlinear system identification in structural dynamics: 10 more years of progress, Mech. Syst. Signal Process. 83 (2017) 2–35, http://dx.doi.org/10.1016/j.ymssp.2016.07.020.

[43] S.F. Masri, T.K. Caughey, A nonparametric identification technique for nonlinear dynamic problems, J. Appl. Mech. 46 (1979) 433–447.

[44] E. Bonisoli, A. Vigliani, Identification techniques applied to a passive elasto-magnetic suspension, Mech. Syst. Signal Process. 21 (2007) 1479–1488, http://dx.doi.org/10.1016/j.ymssp.2006.05.009.

[45] A. Cammarano, S.G. Burrow, D.A.W. Barton, Modelling and experimental characterization of an energy harvester with bi-stable compliance characteristics, Proc. Inst. Mech. Eng. I 225 (2011) 475–484, http://dx.doi.org/10.1177/0959651811403093.

[46] D. Rizos, G. Feltrin, M. Motavalli, Structural identification of a prototype pre-stressable leaf-spring based adaptive tuned mass damper: Nonlinear characterization and classification, Mech. Syst. Signal Process. 25 (2011) 205–221, http://dx.doi.org/10.1016/j.ymssp.2010.07.001.

[47] J.P. Noël, L. Renson, G. Kerschen, Complex dynamics of a nonlinear aerospace structure: Experimental identification and modal interactions, J. Sound Vib. 333 (2014) 2588–2607, http://dx.doi.org/10.1016/j.jsv.2014.01.024.

[48] D. Anastasio, A. Fasana, L. Garibaldi, S. Marchesiello, Nonlinear dynamics of a Duffing-like negative stiffness oscillator: Modeling and experimental characterization, Shock Vib. 2020 (2020) http://dx.doi.org/10.1155/2020/3593018.

[49] S.F. Masri, F. Tasbihgoo, J.P. Caffrey, A.W. Smyth, A.G. Chassiakos, Data-based model-free representation of complex hysteretic MDOF systems, Struct. Control Health Monit. 13 (2006) 365–387, http://dx.doi.org/10.1002/stc.147.

[50] S.F. Masri, H. Sassi, T.K. Caughey, Nonparametric identification of nearly arbitrary nonlinear systems, J. Appl. Math. 49 (1982) 619–628.

[51] C.M. Richard, R. Singh, Identification of multi-degree-of-freedom non-linear systems under random excitations by the "reverse path" spectral method, J. Sound Vib. 213 (1998) 673–708.

[52] D.E. Adams, R.J. Allemang, A frequency domain method for estimating the parameters of a non-linear structural dynamic model through feedback, Mech. Syst. Signal Process. 14 (4) (2000) 637–656, http://dx.doi.org/10.1006/mssp.2000.1292, URL https://www.sciencedirect.com/science/article/pii/S0888327000912925.

[53] S. Marchesiello, L. Garibaldi, A time domain approach for identifying nonlinear vibrating structures by subspace methods, Mech. Syst. Signal Process. 22 (2008) 81–101, http://dx.doi.org/10.1016/j.ymssp.2007.04.002.

[54] C. Martinelli, A. Coraddu, A. Cammarano, Strongly nonlinear multi-degree of freedom systems: Experimental analysis and model identification [data collection], Enl. Res. Data (2023) http://dx.doi.org/10.5525/gla.researchdata.1621.

[55] C. Martinelli, A. Coraddu, A. Cammarano, Experimental parameter identification of nonlinear mechanical systems via meta-heuristic optimisation methods, in: Society for Experimental Mechanics Annual Conference and Exposition, Springer, 2023, pp. 215–223, http://dx.doi.org/10.1007/978-3-031-36999-5_28.

[56] C. Martinelli, A. Coraddu, A. Cammarano, Experimental analysis of a nonlinear piecewise multi-degrees of freedom system, in: International Conference on Nonlinear Dynamics and Applications, Springer, 2023, pp. 665–675, http://dx.doi.org/10.1007/978-3-031-50631-4_56.

[57] A. Cammarano, S.G. Burrow, D.A.W. Barton, A. Carrella, L.R. Clare, Tuning a resonant energy harvester using a generalized electrical load, Smart Mater. Struct. 19 (2010) http://dx.doi.org/10.1088/0964-1726/19/5/055003.

[58] D.J. Ewins, Modal Testing: Theory, Practice and Application, John Wiley & Sons, 2009.

[59] K. Worden, G.R. Tomlinson, Nonlinearity in Structural Dynamics: Detection, Identification and Modelling, CRC Press, 2001.

[60] J.M.W. Brownjohn, A. Pavic, Experimental methods for estimating modal mass in footbridges using human-induced dynamic excitation, Eng. Struct. 29 (11) (2007) 2833–2843.

[61] C.M. Richards, R. Singh, Characterization of rubber isolator nonlinearities in the context of single- and multi-degree-of-freedom experimental systems, J. Sound Vib. 247 (2001) 807–834, http://dx.doi.org/10.1006/jsvi.2001.3759.

[62] K. Worden, Data processing and experiment design for the restoring force surface method, part I: Integration and differentiation of measured time data, Mech. Syst. Signal Process. 4 (1990) 295–319.

[63] E.J. Doedel, A.R. Champneys, F. Dercole, T.F. Fairgrieve, Y.A. Kuznetsov, B. Oldeman, R.C. Paffenroth, B. Sandstede, X.J. Wang, C.H. Zhang, AUTO-07p: Continuation and bifurcation software for ordinary differential equations, 2007.

[64] A. Dhooge, W. Govaerts, Y.A. Kuznetsov, H.G.E. Meijer, B. Sautois, New features of the software MatCont for bifurcation analysis of dynamical systems, Math. Comput. Model. Dyn. Syst. 14 (2008) 147–175, http://dx.doi.org/10.1080/13873950701742754.

[65] H. Dankowicz, F. Schilder, Recipes for continuation, SIAM (2013) URL https://epubs.siam.org/doi/book/10.1137/1.9781611972573.

[66] E.J. Doedel, R.C. Paffenroth, H.B. Keller, D.J. Dichmann, J. Galán-Vioque, A. Vanderbauwhede, Continuation of periodic solutions in conservative systems with application to the 3-body problem, Int. J. Bifurcation Chaos 13 (2003) 1353–1381, URL https://www.researchgate.net/publication/284686576.